THESIS

INTERACTIONS BETWEEN THE MADDEN-JULIAN OSCILLATION AND MESOSCALE TO GLOBAL SCALE PHENOMENA

Submitted by

Benjamin A. Toms

Department of Atmospheric Science

In partial fulfillment of the requirements

For the Degree of Master of Science

Colorado State University

Fort Collins, Colorado

Summer 2019

Master's Committee:

Advisor: Susan C. van den Heever

Elizabeth A. Barnes
Eric D. Maloney
Daniel Cooley

ABSTRACT

INTERACTIONS BETWEEN THE MADDEN-JULIAN OSCILLATION AND MESOSCALE TO GLOBAL SCALE PHENOMENA

The Madden-Julian Oscillation (MJO) influences and interacts with atmospheric phenomena across the globe, from the tropics to the poles. In this two-part study, the interactions of the MJO with other phenomena across a broad range of scales are considered, including mesoscale convective structures within the tropics and global teleconnection patterns. While the two studies are distinct in the scales of the interactions they discuss, each highlights an aspect of the importance of interactions between the MJO and variability across a broad range of scales within the climate system. The study of such cross-scale interactions is important for understanding our climate system, as these interactions can transfer energy between phenomena of starkly different spatial and temporal scales.

Part one of the study uses a cloud-resolving model, the Regional Atmospheric Modeling System, to consider the relationship between mesoscale convective structures within the Indo-Pacific region and the regional, intraseasonal anomalies associated with the MJO. The simulation captures the entirety of a canonical boreal summertime MJO event, spanning 45 days in July and August of 2016, during which the convective anomaly associated with the MJO propagated over the Maritime Continent. The convective cloud structures, or cells, within the simulation were tracked and logged according to their location relative to the regional convective anomaly of the MJO. Using both spectral analysis and phase compositing, it was found that a progressive relationship exists between the boreal summertime MJO and mesoscale deep convective structures within the Indo-Pacific region, specifically within the convectively enhanced region of the MJO, as follows: increased cell longevity in the initial phases of the MJO, followed by increased cell number in the intermediate phases, progressing into increased cell expanse in the terminal phases. This progres-

sive relationship is connected back to the low-frequency atmospheric response to the MJO. It is suggested that the bulk thermodynamic and kinematic anomalies of the MJO are closely related to the convective cell expanse and longevity, although the number of convective cells appears to be tied to another source of variability not identified within this study. These findings emphasize that while the MJO is commonly defined as an intraseasonal-scale convective anomaly, it is also intrinsically tied to the mesoscale variability of the convective systems that constitute its existence.

The second part of the study quantifies the prevalence of the MJO within the overall climate system, along with the dependence of its teleconnections on variability in another tropical phenomena on a larger scale than itself. It is well known that the MJO exhibits pronounced seasonality in its tropical and global signature, and recent research has suggested that its tropical structure also depends on the state of the Quasi-Biennial Oscillation (QBO). We therefore first quantify the relationship between 300-mb geopotential anomalies and the MJO across the globe, then test the dependence of the relationship on both the meteorological season and the QBO phase using a derivative of cross-spectral analysis, magnitude-squared coherence (Coh^2). It is found that the global upper-tropospheric signature of the MJO exhibits pronounced seasonality, but also that the QBO significantly modulates the upper-tropospheric tropical and extratropical anomalies associated with the MJO. Globally, variability in upper tropospheric geopotential linked to the MJO is maximized during the boreal summertime and wintertime of easterly QBO phases, which is consistent with previous research that has shown easterly QBO phases to enhance the persistence of tropical convection associated with the MJO. Additional features are identified, such as the global maximum in upper-tropospheric variability associated with the MJO occurring during boreal summertime, rather than boreal wintertime. Overall, the MJO explains seven to thirteen percent of intraseasonal atmospheric variability in 300-mb geopotential, depending on season and QBO phase. These results highlight the importance of considering the phase of the QBO in analyses related to either global or local impacts of the MJO, along with the importance of cross-scale relationships, such as those between the MJO and QBO, in governing the coupling between the MJO and teleconnections across the globe.

This thesis considers the relationship between the MJO and processes that operate on both longer and shorter timescales than itself, including tropical convection and the Quasi-Biennial Oscillation. In doing so, this work highlights the importance of considering relationships between the MJO and atmospheric phenomena on different spatial and temporal scales and with origins distinct from the MJO itself. While theories exist describing the MJO as its own distinct entity, this research corroborates the idea that it is at its core fundamentally linked to the rest of the climate system, both modulating and being modulated by a broad range of atmospheric processes.

ACKNOWLEDGEMENTS

This thesis represents the combined effort of dozens of people who contributed to my development as a scientist over the past two years, and whether your contributions were direct or indirect, I appreciate all of the time that you have invested in me. First, I would like to thank everyone within the Colorado State University Department of Atmospheric Science who contributed to my last two years within the department for making my time as an M.S. student so rewarding. This extends from my classmates who reminded me that friendship is just as important as professionalism, to the front office staff who made all of the logistics seem trivial, and to my advisor and committee who always challenged me to be a better scientist. Particularly, thank you to Sue van den Heever for supporting my ambitions over the past two years, both within the bounds of this thesis and my intellectual explorations into other topics. The van den Heever group as a whole has been patient and supportive of my research over the past two years, from help with learning RAMS to challenging me to uphold the high scientific standards within our group and department, and I thank you all for everything you have done for me. Libby Barnes and Eric Maloney, thanks for contributing so substantially to this thesis and my overall development as a scientist over the past two years. Your involvements have gone well beyond those required for committee members, and I am sincerely thankful. And thank you, Dan Cooley, for introducing me to classical statistics and reminding me that interdisciplinary education has immense benefits.

Thanks to my parents, Ed and Robin, and my brother, Ray, for always supporting my dreams over the past twenty five years and for your help opening doors so I can pursue my career in atmospheric science. My friends and family have taught me that the most important piece of being a successful person in this world is not your own professional achievements, but how you support the ambitions and happiness of those around you, and for that I am infinitely thankful.

Finally, thanks to the atmospheric science community at large for constantly pushing the envelope of our understanding of the world in which we live.

This work was financially supported in part by the Office of Naval Research grant N00014-16-1-3093 and was otherwise supported by the Department of Energy Computational Science Graduate Fellowship via grant DE-FG02-97ER25308 and a graduate fellowship from the American Meteorological Society.

TABLE OF CONTENTS

LIST OF TABLES

LIST OF FIGURES

Chapter 1

Introduction

1.1 The Madden-Julian Oscillation

Deep convective structures populate the tropics, providing the energetics that drive the large-scale tropical circulation and interacting with superimposed atmospheric disturbances (Chang 1995; Fierro et al. 2009; Hendon and Liebmann 1991; Kiladis and Weickmann 1992; Lane et al. 2001). While waves that propagate independently from convection are essential to the definition of the tropical atmosphere (Dunkerton 1991; Liebmann and Hendon 1990; Majda and Stechmann 2009), this thesis focuses on waves that are coupled with deep tropical convection. Waves that have been theoretically derived as dry modes have been shown to occasionally become coupled to convection, especially within the tropics. Prime examples of such waves include convectively coupled mixed-Rossby gravity waves (Chang and Miller III 1977; Wallace 1971; Yanai et al. 1968; Zangvil and Yanai 1980, 1981) and Kelvin waves (Roundy 2008; Straub and Kiladis 2002, 2003; Wheeler et al. 2000), the former of which has a period of approximately two to six days, while the latter may have periods ranging from days to weeks (Wheeler and Kiladis 1999). While convectively coupled mixed-Rossby gravity waves and Kelvin waves commonly populate the tropics, a more dominant convectively coupled wave pattern exists, defining its own spatial and temporal scale and interacting with convective coupled waves on smaller scales. This wave, the Madden-Julian Oscillation (Madden and Julian 1971, 1972, 1994), has captured the attention of researchers for decades, with scientists debating its formation and propagation mechanisms, the importance of cross-scale relationships throughout its life-cycle, and its impact on the global circulation.

The Madden-Julian Oscillation (MJO) is commonly defined as a global-scale wave, with a wavenumber 1 or 2 longitudinal extent within the tropics (Adames and Kim 2016a). Within its tropical extent, disturbances of varying spatial and temporal expanse generate and decay, ranging in scale from tens of kilometers in the form of isolated convective towers to thousands of kilome-

ters in the form of convectively coupled Kelvin waves. The MJO is, at its core, a phenomenon that spans across multiple spatial and temporal scales, and a growing body of research has shown that the multi-scale structure of its convective interior is important to the evolution of its spatial character. Numerous studies have targeted down-scale influences of the MJO, from which it has been suggested that the MJO may modulate other convectively coupled waves, the diurnal cycle (Peatman et al. 2014a), and even isolated deep convection (Barnes and Houze Jr 2013b; Hendon and Liebmann 1994a; Xu and Rutledge 2014; Zuluaga and Houze Jr 2013a). Beyond the tropics, the MJO teleconnects across a similarly broad range of scales, modulating the frequency and intensity of tropical cyclones (Hall et al. 2001; Klotzbach 2010; Liebmann et al. 1994; Maloney and Hartmann 2000), atmospheric rivers (Baggett et al. 2017; Guan and Waliser 2015; Mundhenk et al. 2016, 2018), and severe weather within the United States (Baggett et al. 2018), and the occurrence of other Rossby wave-driven weather patterns within the midlatitudes (Cassou 2008; Henderson et al. 2016a; Zhang 2013).

The structure and global influences of the MJO exhibit pronounced seasonality (Madden 1986a; Wu et al. 2006; Zhang and Dong 2004). During boreal wintertime, the MJO is equatorially centered and generally propagates directly towards the east, whereas during boreal summertime the convective anomaly exhibits off-equatorial propagation after initiation within the Indian Ocean, extending from the southeast toward the northwest as it interacts with the Maritime Continent. Various mechanisms for the seasonality in the MJO have been proposed, including an explanation that generalizes the modern moisture-mode MJO theory to both boreal summertime and wintertime (Adames and Kim 2016b; Jiang et al. 2018). Namely, the unified theory suggests that the propagation of the MJO relies on intraseasonal gradients in atmospheric water vapor, which change orientation between seasons. However, a consensus has not yet been reached on a satisfactory theory of the MJO regardless of season (Ling et al. 2017), and additional studies of the importance of cross-scale interactions are thereby still warranted to better understand the fundamental character of the MJO. The cross-scale interactions of the MJO are also variable across seasons, with the boreal summertime MJO interacting more directly with the Indochina peninsula and the

northern extents of the Maritime Continent. The diurnal cycle is magnified within this region relative to the equatorial Pacific by the islands sprinkled throughout its interior and the Indochina landmass (Nesbitt and Zipser 2003; Peatman et al. 2014b; Rauniyar and Walsh 2011; Yang and Slingo 2001), and easterly waves frequent its northern extent during boreal summertime (Ritchie and Holland 1999). It is not yet very well understood whether the difference in these cross-scale interactions is important to the seasonality in the global-scale structure of the MJO.

The tropical and global structure of the MJO is dependent on the background state of the atmosphere. The Quasi-Biennial Oscillation (QBO) is a periodic tropical phenomenon and takes the form of a reversal in zonal wind anomalies within the lower tropical stratosphere approximately every 28 months (Baldwin et al. 2001) and has been shown to substantially modulate the MJO (Lee and Klingaman 2018; Son et al. 2017; Zhang and Zhang 2018). The QBO is driven by the depositing of easterly and westerly momentum into the stratosphere by an amalgamation of tropical waves, ranging from convectively generated inertial gravity waves on the scale of tens to hundreds of kilometers to Kelvin waves with scales of thousands of kilometers (Kawatani et al. 2010; Lindzen and Holton 1968). Numerous studies have shown the QBO to modulate the boreal wintertime MJO. For example, the seasonal average amplitude of the tropical top-of-atmosphere longwave radiative response to the MJO is approximately doubled during easterly QBO states relative to westerly QBO states, in part due to longer lasting MJO events (Son et al. 2017; Zhang and Zhang 2018). Additional linkages between the MJO and QBO are found within the extratropics, wherein the influences of the MJO on the North Pacific storm track is modulated by the QBO, with easterly QBO phases favoring a more longitudinally expansive and intense storm track (Wand et al. 2018). Within the eastern Atlantic, landfalling atmospheric rivers are also modulated by the MJO and QBO, although the relationship depends on the location being considered (Baggett et al. 2017; Mundhenk et al. 2018). It has thus become apparent that the QBO is a substantial modulator of both the tropical and extratropical characteristics of the MJO. Furthermore, the QBO represents a downscale influence imposed on the MJO, of which there are few given the relatively long timescale of the MJO itself.

1.2 Experiment Objectives and Key Findings

This thesis is split into two research components, each of which targets a particular scale interaction of the MJO. While the focus of the subsequent analyses and discussions is on the scientific objectives of the two studies, emphasis is also placed on the methods used to conduct the studies. For the first study, cloud-resolving simulations are paramount to the conclusions that are drawn, while in the second study cross-spectral analysis enables encompassing statements about the global structure of the MJO. The purpose of this thesis is to both highlight the importance of the particular methods in the ultimate scientific discoveries and to analyze the output of the numerical and statistical techniques using a critical, scientific approach.

The second chapter investigates the relationship between deep convective structures and the boreal summertime MJO using a cloud-resolving model. As discussed within the introduction, the prevalence of cross-scale relationships within the MJO is still not clearly understood, and this study thereby targets the cross-scale relationships between the regional convective anomaly of the MJO and the individual convective cells that constitute its tropical existence. Cloud-resolving models (CRMs) explicitly resolve the mesoscale structure of cloud systems and thereby offer an opportunity to directly examine relationships between clouds and larger-scale phenomena such as the MJO. CRM simulations offer statistical relationships between convective morphology and the MJO along with the ability to tie these relationships back to the physics of the atmosphere, such as through the thermodynamic and kinematic state of the atmosphere. Methods other than CRMs do not permit a comprehensive evaluation of the mesoscale convective structure of the MJO. For example, reanalysis lends gridded information about the thermodynamic and kinematic state of the atmosphere, but does not directly capture the mesoscale variability within the MJO and rather must indirectly represent its influences using sub-grid scale parameterizations. Satellites, on the other hand, offer observational data regarding the characteristics of mesoscale cloud structures, but typically do not include neither 3-dimensional cloud information nor information regarding the state of the atmosphere that led to the generation of the cloud structures. The CRM is therefore

a critical tool for investigating the relationship between convective structures and the MJO in a comprehensive manner.

The main results of this first study are the following: 1) a progressive relationship between the MJO and convective cell morphology exists within the active lobe of the MJO, 2) no progressive relationship exists between the MJO and convective cell morphology within the suppressed lobe of the MJO, and 3) bulk thermodynamic and kinematic variables suggest that the derived relationships are tied to physical relationships between convection and the MJO and do not depend on the choice of statistical analysis technique. The progressive relationship between the MJO and convective cell morphology proceeds as follows: increased cell longevity in the initial phases, followed by increased cell number in the intermediate phases, progressing into increased cell expanse in the terminal phases. This progressive relationship exists on subseasonal timescales, but is apparent within the overall evolution of convective cells and accounts for approximately ten to twenty percent of all variability in convective cell morphology documented within the simulation. The bulk thermodynamic and kinematic characteristics of the atmosphere seem to most influence convective cell expanse and longevity, although the number of convective cells appears to be tied to another source of variability not identified within this study. This work was completed in collaboration with Susan C. van den Heever, Emily M. Riley Dellaripa, Stephen M. Saleeby, and Eric D. Maloney, and is in preparation for submission to the *Journal of the Atmospheric Sciences*.

In the third chapter the global upper-tropospheric geopotential anomalies associated with the MJO and their seasonality and dependence on the state of the Quasi-Biennial Oscillation (QBO) is investigated. While previous studies have begun to tease apart the relationship between the tropical structure of the MJO and the QBO (Hendon and Abhik 2018; Son et al. 2017), a comprehensive global evaluation of their relationship has not yet been published according to our knowledge. We therefore ask whether the global response to the MJO, through both its tropical character and extratropical teleconnections, depends on the state of the QBO, and if so to what extent? Cross-spectral analysis is used as the primary tool within this study, as it offers a robust estimation of the relationship between two periodic time series. Magnitude-squared coherence (Coh^2), a derivative

of cross-spectral analysis, can be interpreted as the fraction of variability in a periodic time series, y, that can be explained by variability in another time series, x, across each individual harmonic mode. The fraction of variability in upper-tropospheric geopotential that can be linked to the MJO is thereby estimated using Coh^2, which provides context for the MJO within the overall climate system.

It will be shown that: 1) the global teleconnections of the MJO depend on both the season and phase of the QBO; 2) the global signature of the MJO is most pronounced during boreal summertime and wintertime of easterly QBO states; 3) the MJO accounts for six to thirteen percent of variability in upper-tropospheric geopotential depending on season and QBO phase. These findings are linked back to physical mechanisms proposed by other studies. For example, the more prominent global prevalance of the MJO during easterly QBO phases is consistent with the more persistent tropical convective anomaly of the MJO during these periods. Additional nuanced characteristics of the global MJO pattern are also discussed, including the more coherent tropical signature of the MJO during boreal summertime compared to boreal wintertime. It is suggested that the increased summertime coherence is due to either the more pronounced convection within the Eastern Pacific associated with the MJO during boreal summertime, which may preserve its tropical equatorial structure further east than is observed during boreal wintertime, or the prominent westerly wave duct that exists during boreal wintertime within the eastern Pacific (Webster and Holton 1982) that may interfere with the eastward propagation of the MJO within this region. This work was completed in collaboration with Elizabeth A. Barnes, Eric D. Maloney, and Susan C. van den Heever, and is in preparation for submission to the *Journal of Climate*.

The remainder of this thesis is structured according to the findings of the two separate studies. Each chapter includes its own introduction, methodology, discussion, and conclusion sections, and may serve as stand-alone monologues. In chapter 2, the cloud-resolving simulation of the boreal summertime MJO and the associated conclusions regarding the cross-scale relationships between convective cell morphology and the regional anomalies of the MJO are detailed. The global scale upper-tropospheric teleconnections of the MJO and its dependence on both season and QBO phase

are quantified in chapter 3. Finally, the findings of this thesis are summarized and suggestions for future work are made in chapter 4.

Chapter 2

The Relationship Between the Boreal Summertime Madden-Julian Oscillation and Tropical Deep Convective Morphology

2.1 Introduction

Deep convective structures populate the tropics, providing the energetics that drive the large-scale tropical circulation and interacting with superimposed atmospheric waves (Chang 1995; Fierro et al. 2009; Hendon and Liebmann 1991; Kiladis and Weickmann 1992; Lane et al. 2001; Lorenz 1969; Riehl and Malkus 1957). The Madden-Julian Oscillation (MJO; Madden and Julian (1971, 1972, 1994); Zhang (2005)) is one such disturbance, and while the MJO is commonly defined according to its convective anomaly, its intraseasonal temporal scale and global spatial scale are substantially greater than that of typical mesoscale convective anomalies. How intimate of a relationship do deep convective structures hold with the MJO? To what extent do convective structures, meandering about the tropics, dynamically interact with the planetary-scale structure of the MJO? These questions have been popular topics of debate for decades, and as computational and observational capabilities have improved over recent years, the ability to directly investigate them has similarly improved in tandem.

The MJO is an episodic disturbance within the equatorial tropics with a period of 30 to 80 days and can be defined by two distinct modes of variability, one during boreal summertime and another during boreal wintertime (Madden 1986b; Wu et al. 2006; Zhang 2005; Zhang and Dong 2004). Historically, a plethora of research has focused on the characteristics of the wintertime form of the MJO or has considered the MJO to have consistent characteristics throughout the entire year (Hendon and Salby 1994; Wheeler and Hendon 2004). Recent research has emphasized that the consideration of the seasonality of the MJO is important both for developing real-time proxies for

its location and magnitude and for process-based studies (Jiang et al. 2018; Kikuchi et al. 2012a; Kiladis et al. 2014). Within this study, we focus on cross-scale interactions within the summertime MJO, which has been labeled with an assortment of identities, including the boreal summertime intraseasonal oscillation (BSISO; e.g. Kikuchi et al. (2012a); Wang and Xie (1997)), summertime MJO mode (Zhang and Dong 2004), or Indo-Pacific intraseasonal oscillation (Waliser et al. 2004).

While the MJO is commonly defined as a planetary-scale disturbance (Adames and Kim 2016b), it is comprised of a broad range of atmospheric phenomenon with scales ranging from individual convective cells (Barnes and Houze Jr 2013c; Riley et al. 2011; Zuluaga and Houze Jr 2013b) to expansive subtropical Rossby gyres (Kiladis et al. 2005). The convective mode of the MJO can itself be dissected into various constituents. On the largest scale, a convective dipole exists, each pole of which can span thousands of kilometers longitudinally (Wheeler and Hendon 2004) (Figure 2.1). The convective dipole gradually propagates eastward throughout the lifecycle of the MJO, originating within the western Indian Ocean and decaying within the central Pacific Ocean. Within this dipole, synoptic convective anomalies generate and decay, sometimes taking the form of tropical cyclones (Li and Zhou 2013) or eastward propagating inertia-Rossby waves (Yang and Ingersoll 2011). The mesoscales are also prominent (Barnes and Houze Jr 2013a; Vincent and Lane 2018), with convective elements ranging in scale from isolated convective elements to expansive mesoscale convective systems that generate their own sub-synoptic circulations (Hendon and Liebmann 1994b; Johnson and Kriete 1982). These convective elements meander within the regional scale convective envelope, partially driven by the large-scale circulation and partially excited, maintained, and propagated by interactions with surrounding convective elements.

When defined as a convective disturbance, the MJO is at its core an amalgamation of convective elements, each with its own lifespan and identifying characteristics. The lifecycle of each MJO event can therefore possibly be explained as a collection of mesoscale convective events, which interact with each other and any local or upscale background environments they exist within. What information can be gleaned when such a bottom-up approach is taken to interrogating the structure of the MJO? *Rather than considering the MJO as a predominantly downscale-driven convective*

anomaly, what insights can be made by equivalently considering both the mesoscale convective elements and the regional, intraseasonal convective anomalies?

Cloud-resolving models (CRMs) offer the unique capability of capturing the cross-scale interactions within the MJO. By permitting the direct representation of cloud formation, the environments within which clouds form can be analyzed according to the governing physics of the atmosphere, rather than via convective parameterizations as is typically the case in global circulation models (Jiang et al. 2015; Zhang and Mu 2005). The cross-scale interactions between cloud features and the MJO can thereby by directly captured within a CRM, also according to the governing physics of the atmosphere and not those of a convective parameterization. We therefore simulate a canonical summertime MJO event propagating over the Maritime Continent using a CRM to investigate whether any relationships exist between the convective scale and regional scale structures of the summertime MJO. Within the simulation, the lateral boundaries are constrained with reanalysis, but mesoscale and synoptic disturbances are permitted to freely develop within the interior of the domain. This freedom for convective elements to evolve freely within the domain interior permits the interrogation of how the convection interacts with the regional atmospheric response to the MJO. We then use spectral analysis to test the low-frequency relationship between convective characteristics and the MJO, tying the relationship back to atmospheric state variables in a complete hypothesis for the relationship between convective morphology and the summertime MJO.

We first detail the CRM used to conduct the simulation along with characteristics of the simulated MJO event. The relationship between convective morphology and the intraseasonal character of the MJO are then considered using both spectral analysis and phase compositing. Finally, we connect the relationship between the MJO and convective cell morphology back to atmospheric state variables, and propose causal mechanisms for how intraseasonal anomalies in atmospheric thermodynamic and kinematic conditions relate to the convective structure of the MJO.

2.2 Simulation Details

CRMs can directly represent the mesoscale characteristics of clouds without convective parameterizations, which permits an evaluation of how the state of the atmosphere influences the development and evolution of cloud structures. The capability of CRMs to capture the evolution of cloud features on a structured four-dimensional lattice is unique from that of observational data, which are typically inhomogeneous in resolution and sampling frequency. CRMs are thereby a powerful tool for evaluating the complete evolution of atmospheric systems across a broad range of scales, extending toward the smaller scales of atmospheric convection. Of course, this capability is only of scientific interest if the model is representative of the real atmosphere and associated processes. While models should not necessarily be expected to identically reproduce the convective structure of the atmosphere given the chaotic nature of convection, a reliable model should produce statistics similar to observations. The Maritime Continent and tropics in general are devoid of reliable mesoscale observational data such as surface observations and radar imagery, especially compared to mid-latitudinal regions such as the United States and Europe. CRMs are therefore a critical tool for determining the structure of atmospheric phenomena within the tropics, and extend upon the low-level statistics offered by satellite-based observations by also providing information regarding the underlying kinematic and thermodynamic state of the atmosphere.

We use the Regional Atmospheric Modeling System (RAMS; Cotton et al. (2003); Saleeby and van den Heever (2013a)), a CRM with a bin-emulating double moment microphysics scheme, to simulate a canonical summertime MJO event. RAMS has previously been used to simulate the convective details of the boreal wintertime MJO and accurately captures the distribution of convective cell sizes compared to satellite observations, which suggests it is a viable tool for simulating the convective identity of the MJO (Riley Dellaripa et al. 2018). Details of the simulation parameters are listed in Table 2.1, including the grid spacing, microphysical parameterizations, and lateral boundary conditions.

At the beginning of the simulation, the entirety of the domain is initialized using ERA5 reanalysis and strongly nudged for the subsequent day. Thereafter, atmospheric state variables at the

lateral boundaries are nudged toward ERA5 data, while the interior of the domain is permitted to freely evolve according to the physics of the cloud-resolving model (see Table 2.1 for additional details). This ensures that the synoptic-to-regional scale pattern of the MJO event is retained by ERA5 reanalysis through the lateral boundary conditions, while convective elements are permitted to form and evolve freely according to the physics of the cloud-resolving model. The constraint of the lateral boundaries with reanalysis does limit the upscale influences of convection along the boundaries of the domain, although relative freedom from this constraint can be found within the interior of the domain. *The dominance of the cloud-resolving model physics within the interior of the domain is critical to deriving conclusions relating convective morphology to the regional pattern of the MJO. The relative independence of the formation of clouds from the lateral boundary conditions permits the simulation to directly capture the evolution of atmospheric physics on scales ranging from multiple kilometers to thousands of kilometers.* We can thereby analyze how the convective scales of the atmosphere interact with the regional scale anomalies associated with the MJO.

2.2.1 Simulation Domain

The simulation domain is centered over the Maritime Continent and South China Sea (Figure 2.2), over which the most prominent region of the convective dipole of the summertime MJO propagates. For spatial context, the domain encompasses 9,945,600 square kilometers, which is greater than the spatial extent of the United States of America, including Alaska and Hawaii. The orography within the domain is coarsened to the simulation grid, and therefore has a resolution of approximately 4-km, where the orography of each grid point is the average of native 30-arc second ($\sim$ one kilometer) orographic data. During phase 1 of the MJO, a majority of the simulation domain is within the suppressed lobe of the convective dipole (Figure 2.3). As the MJO progresses throughout its phase space, the convectively enhanced lobe propagates north and east throughout the domain and is gradually replaced by the suppressed lobe, such that the entirety of the domain is

within both the convectively enhanced and suppressed regions of the dipole for at least some time throughout the evolution of the MJO.

2.2.2 MJO Event Details

The simulation captures the entire evolution of a canonical summertime MJO event that propagates across the Maritime Continent as a strong convective anomaly. The canonical MJO event was identified using the Outgoing Longwave Radiation MJO Index (OMI; Kiladis et al. (2014)), which explicitly considers the seasonality of the MJO and therefore captures the defining structures of the summertime MJO (as was shown in Figure 2.1). OMI was derived using principal component analysis of eastward-only anomalies in outgoing longwave radiation with periods of 30 to 96 days, and is therefore a proxy of the regional, low-frequency convective identity of the MJO. To be defined as a canonical event, the event must have maintained a strong character (i.e. $>$1-sigma principal component magnitude) throughout the eight-phase MJO phase space.

The entirety of the July/August 2016 MJO event was simulated from inception to demise, which maintained at least a one-sigma convective anomaly from July 8 through August 17 and throughout all eight phases of the OMI phase space (Figure 2.4). The convective anomaly originated within the Indian Ocean and progressively propagated north and eastward across the Maritime Continent and South China Sea. Within visible satellite imagery, it is apparent that a broad range of convective features formed within the convective dipole, including diurnally forced continental convection, maritime mesoscale convective systems, and even a tropical cyclone on the fringe of the Philippines archipelago (images not shown).

2.3 Comparison Between the Simulation and Observations

As previously discussed, the unique capability of cloud-resolving models to capture the evolution of the atmosphere across a four-dimensional x, y, z, t lattice is only scientifically viable if the model reproduces the low order statistics available from observations. We therefore compare the simulation to ERA5 reanalysis and satellite observations to ensure the simulated large-scale

structure of precipitation and atmospheric state variables such as temperature and wind are similar to observationally based analyses.

The regional characteristics of the MJO event, such as zonal wind and precipitation anomalies, are captured well by the simulation (Figure 2.5). 850-mb zonal wind anomalies (U850) are compared between the simulation and ERA5 reanalysis at the locations marked by the red dots in Figure 2.2, which were chosen to compare locations both nearby and distant from the lateral boundaries of the simulation domain. The locations closest to the lateral boundaries are most strongly influenced by the nudging from ERA5, while the locations within the interior of the domain are predominantly governed by the physics of the cloud-resolving model. As should be the case, U850 anomalies deviate most substantially from ERA5 reanalysis in the interior of the domain, where the lateral boundary conditions have the least influence and where the influence of mesoscale and synoptic scale contributions to the zonal wind are captured by the CRM (Figure 2.5). The intraseasonal (i.e. $>$ 20 day periodicity) U850 variability within the simulation aligns well with reanalysis, although the simulation exhibits a slightly dampened amplitude within the interior of the domain. The higher frequency variability of the simulation with periods of less than 20 days deviates more substantially from that of ERA5, which is also to be expected given that we have designed the simulation to permit the free evolution of meso- and synoptic scale disturbances within the interior of the domain. Since the spatial and temporal resolution of the cloud-resolving model is superior to that of ERA5, it would be expected that the statistics of the high-frequency signal from the cloud-resolving model would be more representative of the true atmospheric state and its mesoscale characteristics than would be offered by ERA5 alone.

Observational precipitation data from the Global Precipitation Measurement Mission (GPM; Hou et al. (2014)) depict intraseasonal anomalies in precipitation propagating north and east across the domain throughout the simulation period (Figure 2.6). The northward propagating mode is more well pronounced than the eastward propagating mode, progressing from the southern through northern extents of the domain throughout the simulation period. In the latitudinal-mean Hovmoller, the locations of intraseasonal anomalies appear to zonally oscillate, perhaps due to influ-

ences of island orography. All of these characteristics are also captured well by the simulation (Figure 2.7). Most importantly, the spatio-temporal bounds of the intraseasonal precipitation anomalies with greater than 20 day periodicity align well between the observations and simulation, particularly for the longitudinally averaged Hovmoller diagram. Perhaps the most notable difference between the simulation and observations is the tendency for the simulation to have more intense precipitation over land. The zonal oscillation in intraseasonal precipitation anomalies within the latitudinal-mean Hovmoller are also spatially shifted in the observations relative to the simulation.

The simulation accurately captures the evolution of the MJO event from a regional perspective based on the similarities between the simulated and observed intraseasonal structure of zonal winds and precipitation throughout the simulation period. We therefore use the CRM simulation to analyze the convective structure and mesoscale processes of the MJO event, the details of which are unavailable within either reanalysis or observationally based datasets.

2.4 Convective Tracking Algorithm

We utilize a convective cloud tracking algorithm to generate a database of convective events that occur throughout the simulation. The algorithm is based on thresholds of cloud condensate, precipitation rates, and the fraction of grid cells associated with one convective feature that overlaps other convective cells in sequential time steps. Briefly, the logic of the algorithm is as follows:

1. T = 0; Identify all contiguous regions of cloud (i.e. cloud condensate greater than 0.001 kg kg^{-1}) that are also associated with a surface precipitation rate greater than 5 mm hr^{-1}

2. T = 0 + dt; Identify all contiguous regions of cloud (i.e. cloud condensate greater than 0.001 kg kg^{-1}) that are also associated with a surface precipitation rate greater than 5 mm hr^{-1}

3. Link the convective cloud elements identified in steps 1 and 2 by considering clouds that overlap with a fraction greater than 0.75 to be the same convective element evolved across time

4. Repeat steps 2 and 3 for the remainder of the simulation

The tracking algorithm is not particularly sensitive to the thresholds if values ± 25 percent of those presented in this paper are used, and the qualitative conclusions we draw at the end of the paper are therefore independent of the selection of the threshold values. It is important to note that since all identified cloud objects must be associated with a minimum precipitation threshold that is representative of convective cells (Petersen and Rutledge 2001), the subsequent analysis only considers actively precipitating convective clouds and purposely neglects other cloud features, such as non-precipitating cumulus, residual glaciated clouds or stratiform precipitation from decayed convection, and other general types of non-precipitating clouds.

An example convective cloud feature identified by the algorithm is shown in Figure 2.8. Within this particular case, multiple cell mergers and splits can be observed, along with a shallow arcing band of cloud that is likely associated with the cold pool of the convective cell. In the case of a cell split, a new cell label is created for the cell that least overlaps with the cell structure from the previous time step, while the other cell that most overlaps with the original cell maintains the original label. Based on a clustering of cloud features identified by the convective cloud feature tracking algorithm, the algorithm captures convective structures with a broad range of spatial and temporal characteristics, ranging from isolated, transient convective cells to expansive, persistent mesoscale convective systems (clustering data not shown). In total, 180,000 convective elements were identified within the simulation, spanning a broad range of spatio-temporal character.

Figure 2.9 shows the tracks for each convective cell identified within the simulation, along with the maximum size each convective cell achieved. Of note, the algorithm only tracks convective features that are at least 100 km away from the lateral boundary of the domain to limit any potential contamination caused by the lateral boundary nudging. The spatial pattern of convective tracks produced by the simulation is similar to the July and August convective climatology of the region (Biasutti et al. 2012). Two pronounced regions of convective minima exist: one within the north-central South China Sea and the other between the southern tip of the Philippines and Borneo. The minimum within the South China Sea is associated with a rain shadow induced by winds flowing down the slope of the elevated topography on the eastern coast of Indochina (Wang 2002;

Xu et al. 2008). Numerous convective maxima are also present, the most pronounced of which are atop eastern Indochina, west of the Philippines archipelago within the eastern fringes of the South China Sea, east of the Philippines archipelago within the Philippines Sea, atop Borneo, and along the southern fringes of the South China Sea. The maximum west of the Philippines archipelago is associated with the offshore propagation of diurnally driven convection (Love et al. 2011), while the convectively active region over eastern Indochina is similarly associated with both a persistent diurnal cycle and monsoonal flow within the broader southeast Asian monsoon (Zhang et al. 2002). Within the Philippine sea, easterly waves propagating towards the Maritime Continent excite convection of various modes including two tropical cyclones (not shown) (Ritchie and Holland 1999), while the banding structure along the southern periphery of the South China Sea results from a tail of convection that forms on the southwest side of the aforementioned tropical cyclones. The simulation accurately captures the climatological convective response of the Maritime Continent, and thereby provides a lucrative opportunity for investigating the modulation of the background convective morphology by the MJO.

2.5 Low-Frequency Convective Evolution

We analyze the relationship between the boreal summertime MJO and convective cell longevity, volume, and cell number using two methods. For the first method, spectral filtering of time series of the median values of these three cell characteristics is used to explicitly remove any patterns not directly associated with the intraseasonal timescales of the MJO. The results of the spectral filtering are then corroborated by compositing the convective characteristics into two-dimensional histograms according to MJO phase.

Both of these methods have inherent strengths and weaknesses. The spectral filtering method permits the direct examination of intraseasonal variability associated with the MJO, removing any higher frequency anomalies such as tropical cyclones that may not be directly associated with the MJO. On the other hand, this may be disadvantageous since the MJO has been shown to be linked to higher frequency phenomena such as tropical cyclones, and spectral filtering therefore may not

fully account for cross-scale relationships between the MJO and convective characteristics. Any integrated effects of tropical cyclone activity on the evolution of the intraseasonal character of the MJO event would, however, still be captured by the spectral analysis. This limitation of spectral filtering is mediated by compositing convective characteristics by phase and including anomalies that occur across all spatial and temporal scales. By comparing the results from the spectral filtering and compositing methods, we can be more confident that any relationships derived from either method are robust.

2.5.1 In Frequency Space

For the frequency-based analysis, we generated time-series of convective characteristics for the enhanced and suppressed regional convective anomalies of the MJO prior to spectral filtering. That is, we separated the analysis into the regions of the MJO that are characterized by increased OLR anomalies, which are associated with suppressed convection, and decreased OLR anomalies, which are associated with enhanced convection. For example, for the enhanced regional convective anomaly, we only considered convective features that resided within the convectively enhanced, or negative OLR anomaly, portion of the MJO for each respective day, as defined by OMI. We then calculated the number of cells, median convective cell longevity, and median volume for each ten-minute period of the simulation. The median convective cell longevity for each ten-minute period was calculated by finding the median longevity of all cells, including their lifespan before and after the specified ten-minute period. This generates a single time series for each of the three variables for the convectively enhanced portion of the MJO's convective dipole. The mean is then removed from each time series to generate anomalous time series for each variable, effectively filtering out the background state of the atmosphere. These anomalous time series are then spectrally filtered, and harmonics with periods of less than 20 days are removed. The predominant signal within the 20+ day periods are those associated with the MJO since the summertime MJO accounts for approximately 60 percent of intraseasonal ($>$ 20 day) convective variability within the tropics

(Kiladis et al. 2014). We follow this process for both the convectively enhanced and suppressed regions of the MJO.

Figures 2.10 and 2.11 present the relationship between convective characteristics and the intraseasonal scales of the boreal summertime MJO for the convectively enhanced and suppressed regions, respectively. These figures are presented in radial space, analogous to the phase spaces used to represent the principal component phase space of the MJO (Kiladis et al. 2014; Wheeler and Hendon 2004). Given that the MJO is in reality an episodic disturbance, the relationship between the convective characteristics and the boreal summertime MJO progresses through its evolution for canonical MJO events, but is not necessarily cyclic. Since we intentionally selected an MJO event that is representative of canonical MJO events, the structure of these figures likely represents a progressive evolution that may be identified within other canonical MJO events.

Within the convectively active lobe, the relationship between the boreal summertime MJO and convective organization proceeds sequentially as follows: increased cell longevity in the initial phases, followed by increased cell number in the intermediate phases, progressing into increased cell volume in the terminal phases (Figure 2.10). The relationship is progressive whereby one pattern gradually blends into the next, with the maxima of the oscillations in each convective characteristic being separated by approximately 120 degrees within the phase space. The convective characteristics within the convective active lobe can thereby be distinctly separated into three distinct regimes. In the first regime during phases 1 through 2, convective cells last longer and are more spatially sparse. The second regime occurs during phases 3 through 6, wherein more convective cells exist, but the cells are anomalously small in volume. The third regime occurs during the latter portions of phase 6 through the demise of the MJO event, and is characterized by anomalously expansive convective cells, but a lesser amount of unique convective features.

The consideration of this intraseasonal relationship in the context of all frequencies of convective variability is critical for justifying its importance for the overall convective evolution within the tropics. Intraseasonal anomalies in cell number account for 22.8%, size for 7.8%, and longevity for 17.3% of all variability with periodicities less than or equal to 40 days, which was the duration

of the simulated MJO event. These percentages represent a lower bound of the impacts of intraseasonal variability on convective characteristics, as additional feedbacks between other cycles (e.g. the diurnal cycle) may exist. The MJO does not constitute all intraseasonal variability within the tropics, however, so at least on intraseasonal timescales, these values represent upper bounds of the influences of the MJO.

Convective cell morphology exhibits less pronounced oscillations within the convectively suppressed regime (Figure 2.11). Generally, no progressive relationship exists for convective cell size and longevity within the suppressed lobe, although the number of cells is increased during phases 1 and 2, and again in phase 8. This relative lack of cycle can be interpreted as the convectively suppressed region generally having a singular convective mode, with the convection within the convectively suppressed regimes maintaining their mean-state characteristics regardless of MJO phase. This is, perhaps, equally as scientifically interesting as the more complex convective evolution within the convectively active regime.

2.5.2 Phase Composites

For the compositing-based analysis, we considered convective anomalies of all frequencies but still separately considered the convectively enhanced and suppressed regions of the MJO. That is, we use the unfiltered time series of convective characteristics that have only had their mean removed, which were constructed as discussed in the previous section. The following procedure describes how the two-dimensional histograms were constructed for the convectively active regime, but the process was identical for the convective suppressed regime. We first identified all convective features that occurred within the convectively enhanced regime for each respective phase, as defined by OMI. Two-dimensional histograms comparing each combination of convective characteristic were then generated for each phase. We also calculated the two-dimensional histograms for all convective features within the convectively enhanced region, regardless of MJO phase, which rendered a singular two-dimensional histogram for the entire MJO event for the convectively enhanced regime. Both the phase-specific histograms and the histogram for the entire MJO event

were normalized by the sum of their respective bins. The anomalous characteristics for each phase were then calculated by dividing the normalized, phase-specific histograms by the normalized histogram for the entire MJO event. These anomalous histograms represent the fractional difference between the convective characteristics of each individual phase and the overall MJO event. The anomalous histograms were then plotted on a logarithmic scale with base 10, which renders fractional difference histograms that show the orders of magnitude difference from the background state for each phase, with negative values denoting a reduction in convective features for a bin and positive values denoting an increase.

The phase composited two-dimensional histograms corroborate the results presented within the frequency-based analysis. While we do not show the two-dimensional histograms since the information is redundant to the previous section, we present the two-dimensional histogram between convective cell depth and cell volume to provide an additional perspective on the convective morphology (Figures 2.12 and 2.13). Within the convectively enhanced region of the MJO, the frequency-based analysis within Section 2.5.1 suggested that convective cells are most expansive during the latter phases of the MJO, namely phases 7 and 8. Figure 2.12 corroborates this pattern, with the most expansive convective cells occurring during phases 7 and 8. While the deepest convective mode that extends to the tropopause is similar between the intermediate and latter phases of the MJO, the expansiveness of the shallow convective mode that extends to the middle troposphere increases during the latter phases. The increased expansiveness of the shallow convective mode suggests that the spectral relationships presented within Figure 2.10 include information about all modes of convection, shallow or deep, and it may therefore be interesting to separate the spectral analysis by convective mode in a future study. For the case of cell volume, it seems that variability in the expansiveness of the shallower mode of convection dominates the signal depicted in the spectral analysis.

Within the convectively suppressed region of the MJO, the relationship between convective cell depth is opposite to that of the convective enhanced region (Figure 2.13). More specifically, the deepest convective cells occur during the intermediate phases of the MJO, whereas relatively

shallower convective cells exist during the early and late phases. Unlike the convectively enhanced region, however, the anomalous convective depth and longevity is not bimodal during the phases characterized by the deepest convection. The convectively suppressed regime is located across the northern South China Sea and Philippines archipelago during the intermediate phases, similar to the location of the convectively enhanced regime during the later phases of the MJO.

2.6 Convection Evolution and Atmospheric State

We investigate the low-frequency evolution of the atmospheric state within the simulation in an attempt to physically explain the relationship derived in Section 2.5.1. The intraseasonal evolution of the atmospheric state is defined similar to the rest of the paper, and we only consider anomalies with periods of greater than 20 days, which are isolated using a bandpass spectral filter. Furthermore, only the atmospheric state at convective initiation is considered since the convective life-cycle is much shorter than the periods of atmospheric anomalies being considered within the spectrally filtered time series ($\sim$ 6 hours for persistent convective systems compared to $>$20 days for the atmospheric anomalies). The atmospheric state at convective initiation is therefore most representative of the atmospheric state throughout the entire convective life cycle, although convection does feedback upon its environment, so the atmospheric state would still likely change throughout the convective lifecycle. The location of convective initiation is defined as the x, y centroid of the convective cells at the first time step they were identified.

The connection between convective cell morphology and intraseasonal variability in the atmospheric state was considered using the bulk parameters of vertical wind shear, convective available potential energy (CAPE), and convective inhibition (CIN). We calculated the low-frequency evolution of these bulk parameters according to the following method. First, low-frequency anomalies in atmospheric state variables such as temperature, water vapor mixing ratio, and zonal and meridional wind were calculated. These low-frequency anomalies were calculated for each grid cell within the x, y, z space. The anomalous time series for each variable were calculated for each grid cell by removing the time-series mean for the duration of the simulation. A bandpass filter was then

applied that removes anomalies with periods of less than 20 days, which resulted in low-frequency time series with intraseasonal anomalies with periods of greater than 20 days.

Vertical wind shear anomalies were then calculated via a second-order finite difference approximation to the vertical gradient in the low-frequency wind anomalies for the zonal and meridional wind components. Surface-based CAPE and CIN anomalies were calculated according to a more complicated procedure. The base-state CAPE and CIN were first calculated for each grid point in the x, y space, which were defined as the CAPE and CIN calculated from the mean temperature and water vapor mixing ratio profiles throughout the entire duration of the simulation. Then, the low-frequency anomalies in temperature and water vapor mixing ratio for each x, y, z grid cell were added to the simulation-mean temperature and water vapor mixing ratio profiles, and the CAPE and CIN values for these perturbed profiles were calculated. The low-frequency CAPE and CIN anomalies were then estimated to be the difference between the CAPE and CIN values for the perturbed profiles and the base-state, simulation mean profiles. This procedure rendered anomalous vertical wind shear, CAPE, and CIN profiles at each location in x, y space for all time steps within the simulation.

Figure 2.14 shows the intraseasonal anomalies in various wind shear parameters, CAPE, and CIN at convective initiation throughout the simulation, within the convectively enhanced region of the MJO. The total wind shear is defined as the shear of the wind magnitude, and the wind magnitude is calculated before taking the vertical gradient. Note that Figure 2.14(d) defines low-level vertical wind shear as the magnitude of the difference between the 1000-mb and 800-mb wind vectors and the mid-level vertical wind shear as the difference between the 800-mb and 400-mb wind vectors. These pressure levels are as defined by LeMone et al. (1998), which found a robust relationship between these definitions of low- and mid-level shear, CAPE, and CIN, and convective evolution within the tropics. While the climatological values of shear and bulk tropospheric instability may change across the domain depending on orography and latitude, this analysis considers intraseasonal anomalies from the simulation mean and thereby ignores any geographical dependences of the climatologies of these quantities.

While shear does climatologically increase toward the northern extent of the domain, the analysis is considering only anomalies from the mean, and the shear anomalies are thereby associated with intraseasonal variability about the climatological mean.

The evolution of the atmospheric state at convective initiation may partially explain the relationships between convective morphology and the MJO presented in Section 2.5. As a reminder, the intraseasonal timescale of convective morphology within the convectively enhanced portion of the dipole proceeds as follows: increased cell longevity in the initial phases, followed by increased cell number in the intermediate phases, progressing into increased cell volume in the terminal phases (Figure 2.10). Within the tropics, atmospheric thermodynamics govern convective longevity and depth, while kinematics govern cell structure (LeMone et al. 1998). For a uniform background environment, decreased low- and mid-level shear encourages isolated convective elements, while a relative increase in either low- or mid-level shear encourages upscale growth. The anomalously expansive convection that occurs during the latter phases of the MJO is therefore likely supported by the relative increase in both low- and mid-level shear during these phases (Figure 2.14(d). It is also possible that the relative reduction in low- and mid-level shear during phases 4 through 6 supports the greater number of convective cells during these intermediate phases, although this relationship is somewhat muddled by the increase in wind shear during phase 3.

The relationship between the evolution of the atmospheric thermodynamic state and convective organization is more robust. Generally, an increase in mid- to upper-level moisture supports longer lasting convection, and reduced stability encourages deeper convective cells that repopulate more readily through cold pool interactions (Barnes and Houze Jr 2013c; LeMone et al. 1998). The reduced stability in the latter phases of the MJO may support the deeper convective cells depicted in Figure 2.12, although during the intermediate phases the increased stability is contradictory to the increase in cell population. It seems that an increase in low- to mid-tropospheric moisture in the early and late phases of the MJO is predominantly responsible for the increased cell longevity during these phases (Figured 2.15). The increased longevity supported by the anomalously high low- to mid-tropospheric moisture content may also contribute to the increased cell volume during these

periods. Should convective cells be maintained for a longer period of time, there is an increased likelihood that the cells can interact with surrounding convective elements and grow upscale. In summary, the relationship between the bulk thermodynamic and kinematic characteristics of the atmosphere seem to best explain the evolution of convective cell volume and longevity, but do not seem to be strongly tied to the number of cells.

2.7 Summary and Conclusions

The Madden-Julian Oscillation exhibits pronounced multi-scale structure, spanning from regional convective anomalies with scales of thousands of kilometers to mesoscale convective features that are best defined by their individual convective updrafts. A plethora of research questions remain unanswered regarding the importance of spatial and temporal scales within the MJO, including how the regional intraseasonal anomalies and individual convective features interact. Cloud-resolving models offer a unique opportunity to capture the entire breadth of scales within the MJO, as they permit the organic development of cloud structures and thereby the direct interpretation of interactions between the meso- and regional scale structures of the MJO. We therefore used a cloud-resolving model to investigate the relationship between convective cell morphology and regional anomalies associated with the MJO.

A canonical boreal summertime MJO event was simulated, which spanned from July 10, 2016 through August 17, 2016 and persisted throughout the entire MJO phase space as a strong convective anomaly (Figure 2.4). The simulation domain was centered over the Maritime Continent and South China Sea, since these regions experience the peak intensity of convective anomalies throughout the MJO lifecycle (Figures 2.1 and 2.2). The lateral boundaries of the simulation were perturbed by ERA5 reanalysis, while the interior of the domain was allowed to freely evolve according to the physics of the cloud-resolving model. This ensured that while the synoptic and regional scale structure of the MJO was maintained by ERA-5 through the lateral boundary conditions, the mesoscale and synoptic identity of the MJO was captured directly by the cloud-resolving

model itself. In doing so, we permitted the direct investigation of how deep convective structures interact with the regional convective anomalies associated with the MJO.

The convective population was sampled using a convective cloud tracking algorithm and then analyzed for its relationship with the intraseasonal character of the MJO. Using the convective cloud tracking algorithm, a total of approximately 180,000 convective cells was identified throughout the simulation, whereby a convective cell was defined as a contiguous expanse of convectively generated cloud that was actively precipitating. We considered the evolution of the convective populations within the MJO convective anomalies according to three characteristics: the number of convective cells, convective cell volume, and convective cell longevity. Time series of these three variables were generated for both the convectively enhanced and suppressed lobes of the MJO, and filtered to include only variability with periods of greater than 20 days. In doing so, the relationship between convective morphology that is coupled with variability on intraseasonal timescales, and thereby likely the MJO, was isolated. We found that a pronounced progressive relationship in convective morphology occurs within the convectively enhanced lobe of the MJO, as follows: increased cell longevity in the initial phases, followed by increased cell number in the intermediate phases, progressing into increased cell volume in the terminal phases (Figure 2.10). Furthermore, the depth of convective cells tends to be greatest during the latter phases of the MJO (Figure 2.12). This evolution is depicted schematically in Figure 2.16. The cell morphology is less dynamic within the convectively suppressed lobe of the MJO, wherein the population of convective cells generally maintains a singular identity throughout the entire life cycle of the MJO. These relationships are apparent within both spectrally filtered time-series of convective number, volume, and longevity, and within 2-dimensional histograms composited by MJO phase.

The relationship between the progressive morphology of the convective population and the low-frequency atmospheric response to the MJO is more complicated. Bulk atmospheric characteristics such as vertical wind shear and convective available potential energy have previously been used to separate environments most conducive for varying types of convective morphology. For example, increased vertical wind shear is favorable for upscale growth, while reduced ver-

tical wind shear and increased convective instability favors a greater number of convective cells (LeMone et al. 1998). We hypothesized that these relationships might also hold for the anomalies in bulk atmospheric characteristics generated by the MJO. In other words, we investigated whether intraseasonal anomalies in wind shear and convective instability dictate the progressive convective morphology within the convectively enhanced lobe of the MJO. In essence, the evolution of intraseasonal anomalies in thermodynamic and kinematic characteristics of the atmosphere seem to most influence convective cell volume and longevity, whereas the number of convective cells appears to be tied to another source of variability not identified within this study.

The discovery of the intraseasonal relationship between the MJO and the evolution of convective cells within the enhanced and suppressed regions of the MJO may have broader implications for the large-scale structure and evolution for the MJO. For example, the distribution of cloud within the dipole of the MJO may relate to the redistribution of water vapor from the boundary layer into the free troposphere, which has been found to be a critical factor in the overall evolution of the MJO on scales associated with convectively coupled equatorial waves (Adames and Wallace 2015). If the mesoscale convection of the MJO is to feedback onto its intraseasonal structure, it may be through the vertical redistribution of water vapor anomalies by deep convection, aggregated onto an intraseasonal structure. It would therefore be interesting to examine whether the mesoscale convective features within the intraseasonal convective anomaly feed upscale into the intraseasonal water vapor anomaly using methods such as spectral flux, as detailed in Arbic et al. (2012) and Hayashi (1980).

The progressive relationship discovered within this study has the potential to be expanded upon by future studies. The causal relationship proposed in this study can be elaborated upon, for example, particularly regarding the relationship between the number of convective cells and MJO phase. The broader implications of this work could also be investigated, including the potential for the discovered intraseasonal relationship between convective morphology and the MJO to contribute to convective parameterizations regarding low-frequency modulation of convective

variability. Generally, this work is supportive of the idea that the mesoscales and intraseasonal timescales are closely coupled within the tropics.

Table 2.1: Simulation parameters

Model Aspect	Setting
Model	Regional Atmospheric Modeling System (RAMS) Version 6.2.07
Grid	Arakawa C grid
	Δ x = Δ y = 4 km; 3360 km longitudinal extent; 2920 km latitudinal extent
	Δ z varies with height
	surface Δ z = 100m; domain top Δ z = 1000m
	vertical stretch ratio = 1.10
	42 vertical levels; model top 25.5 km
Time integration	8 s time step
	40 day simulation (July 8, 2016 through August 17, 2016)
Initialization	ERA-5 domain-wide initialization
	Central nudging with 4 hour damping (τ = 14,400 s) for first day of simulation
	Initial time of July 8, 2016 at 00z
Surface scheme	Sea-surface temperatures (SST) constrained by Reynolds SST observational data set (Reynolds et al. 2002)
	Soil moisture nudged to ERA-5 with 4 hour damping
	Climatological NDVI representing continental vegetation
Boundary conditions	Open radiative lateral and upper boundaries (Klemp and Wilhelmson 1978)
	Lateral and upper boundary nudging to ERA-5 with 30 minute damping (τ = 1800 s) for entirety of simulation
	20 outermost grid cells along lateral boundaries
	from 20 km to upper boundary
Microphysics scheme	Two-moment bulk microphysics (Meyers et al. 1997)
	Eight hydrometeor classes (Saleeby and Cotton 2004)
Radiation scheme	Harrington (Harrington 1997) two-stream, updated every 30 minutes
Aerosol treatment	Aerosol species: sulfates (Saleeby and van den Heever 2013b)
	No aerosol sources or sinks
	Static (non-advective) aerosol profile
	DeMott et al. (2010) ice nucleation parameterization
Turbulence Scheme	Smagorinsky (1963) sub-grid scale closure

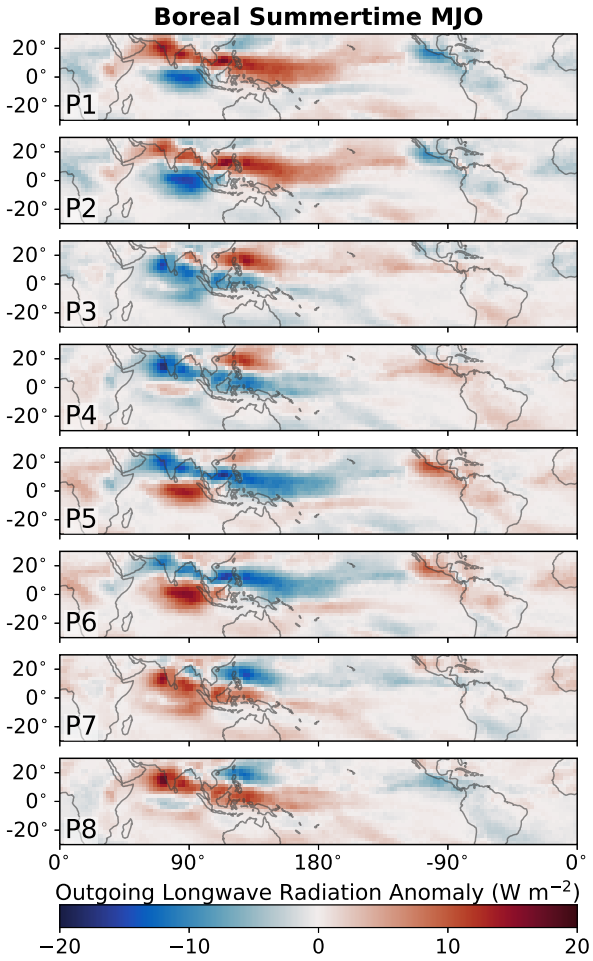

Figure 2.1: Outgoing longwave radiation anomalies associated with the boreal summertime Madden-Julian Oscillation. The anomalies are shown according to the typical eight-phase evolution of the MJO and correspond to a 1-σ principal component magnitude from the Outgoing Longwave Radiation MJO Index (OMI; Kiladis et al. (2014)). The construction of OMI considers the regional, intraseasonal character of OLR anomalies and thereby does not directly consider the mesoscale convective structure of the MJO. Positive (negative) OLR anomalies correspond to suppressed (enhanced) convection.

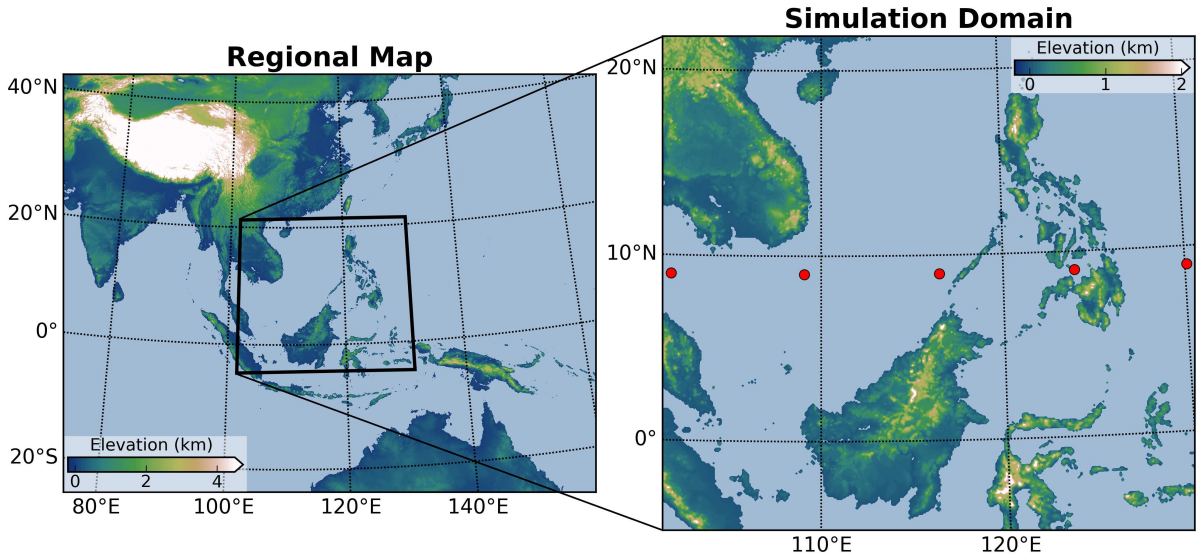

Figure 2.2: (Left) Topographic map of the Indo-Pacific region, with the simulation domain outlined in black; (Right) Topographic map of the simulation domain. The red dots denote the locations where data was extracted for the comparison between RAMS and ERA-5 in Figure 2. Note that the color scales are different between the regional map and the simulation domain. Topography is not extracted from the model, and shows the topography at 30" resolution (approximately 100 meters at the equator).

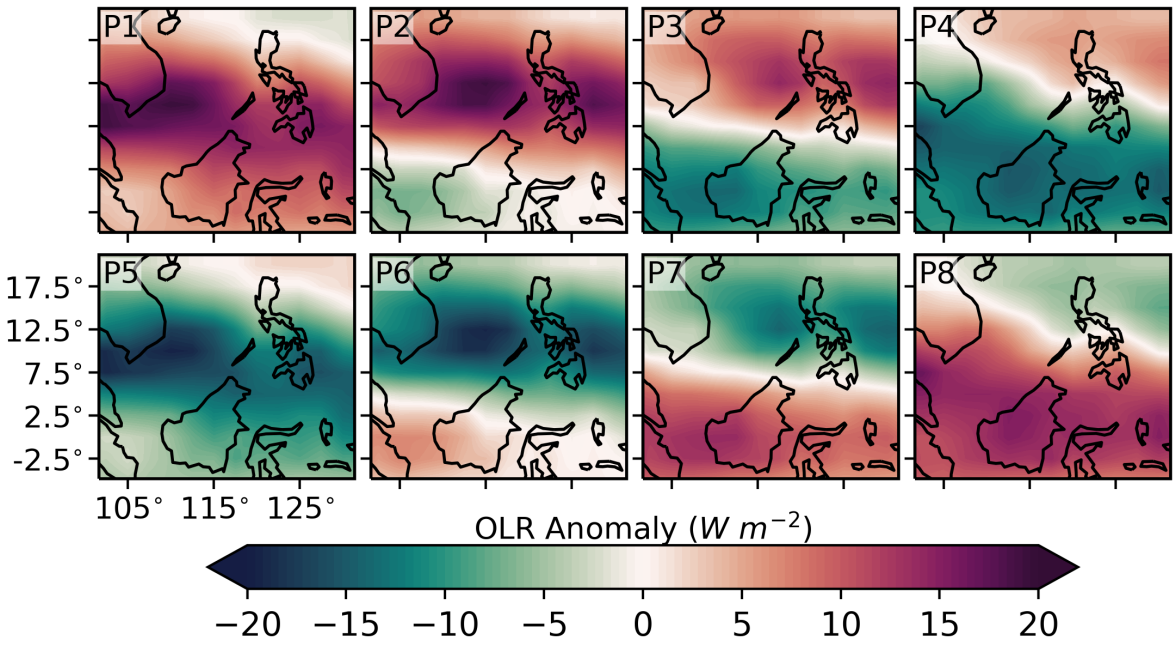

Figure 2.3: Outgoing Longwave Radiation (OLR) anomalies for each phase of a canonical boreal summertime MJO event. Anomalies correspond to a 1-σ MJO event using the OMI EOF patterns for July 31. Green (red) denotes negative (positive) OLR anomalies, which signifies enhanced (suppressed) convection.

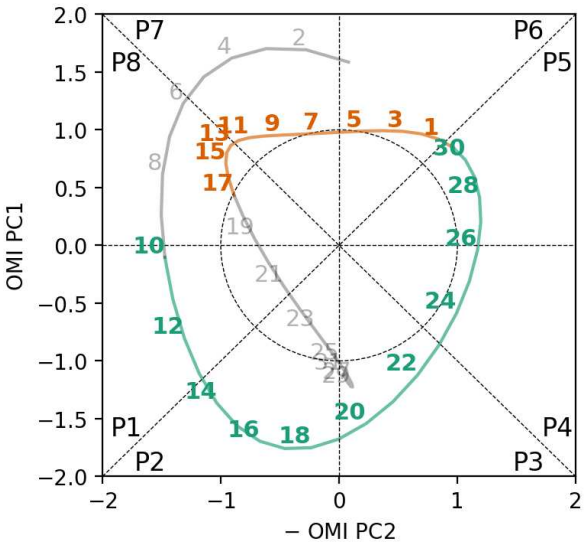

Figure 2.4: OMI principal component phase space for the July/August 2016 boreal summertime MJO event. Dates that were analyzed are colored, while dates outside of the analyzed simulation data are in gray. July dates are colored, green and August dates are colored orange. Note that the principal component ordering has been changed to ensure this phase space diagram can be compared directly to the conventional RMM phase space diagram as originally developed within Wheeler and Hendon (2004).

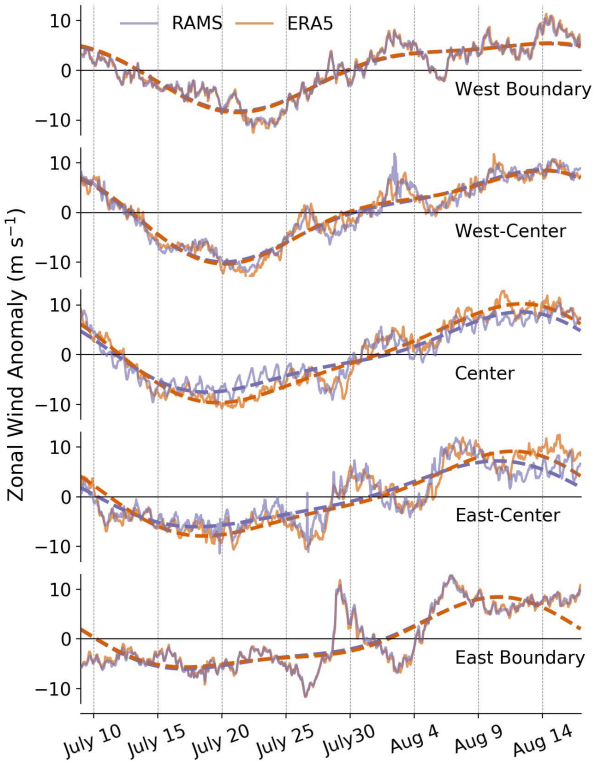

Figure 2.5: Time series of 850-mb zonal wind anomalies for the RAMS simulation and ERA5 across the simulation domain, as labeled by the red dots in Figure 1. The solid lines show the unfiltered time series, while the dashed lines show only 20+ day variability.

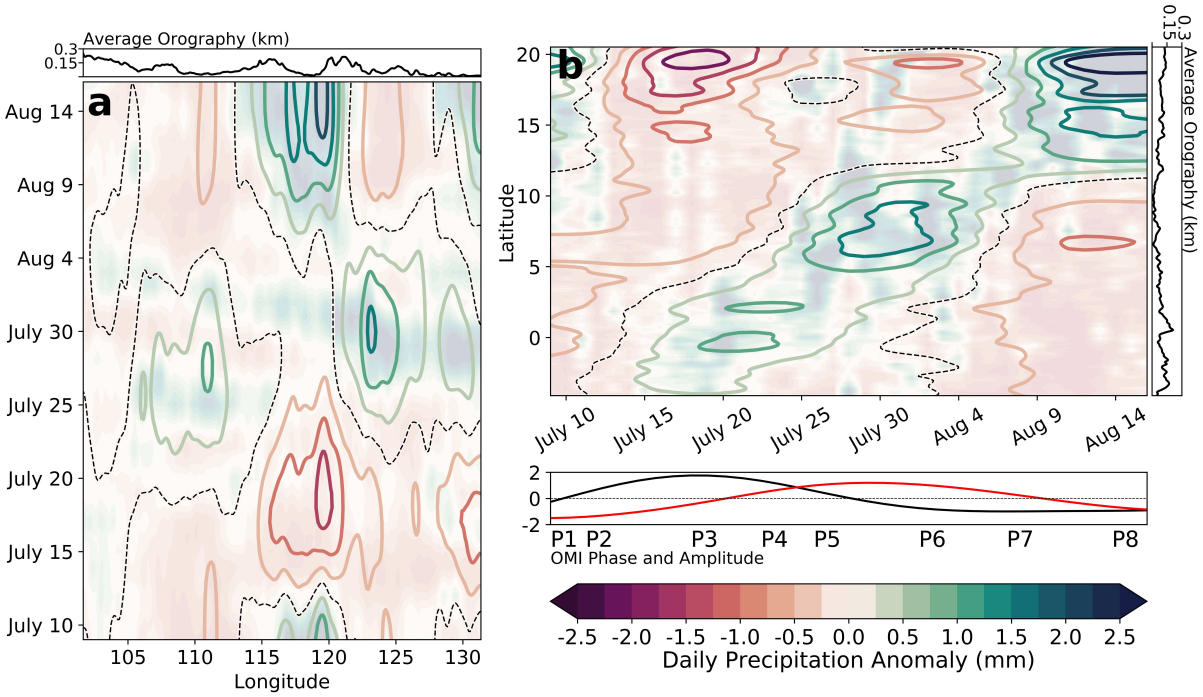

Figure 2.6: (a) Longitudinal and (b) latitudinal Hovmoller diagrams of daily precipitation anomalies across the simulation domain from Global Precipitation Measurement Mission (GPM) observations. (c) OMI principal component time-series with dates corresponding to the x-axis of the latitudinal Hovmoller diagram, with PC1 in black and PC2 in red. The filled background shows the total precipitation anomaly, while the contours show the intraseasonal ($>$ 20 day) precipitation anomalies. The dashed black line denotes the zero contour for the low-frequency anomalies.

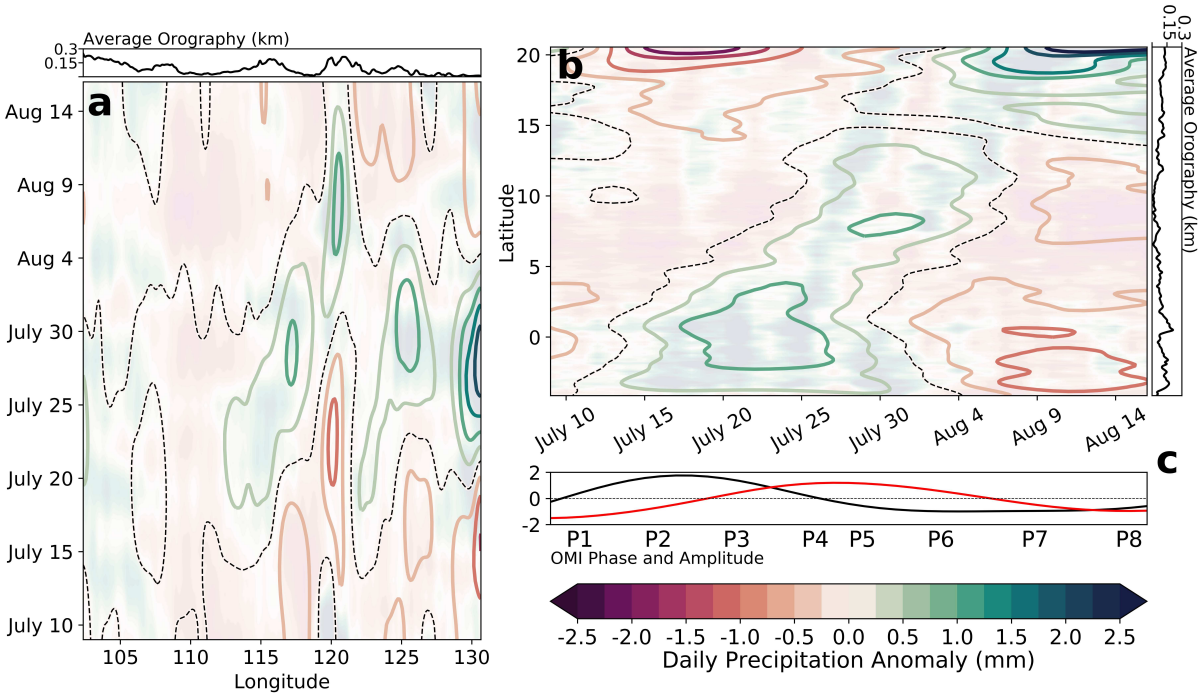

Figure 2.7: As in Figure 2.6 but for the cloud-resolving simulation.

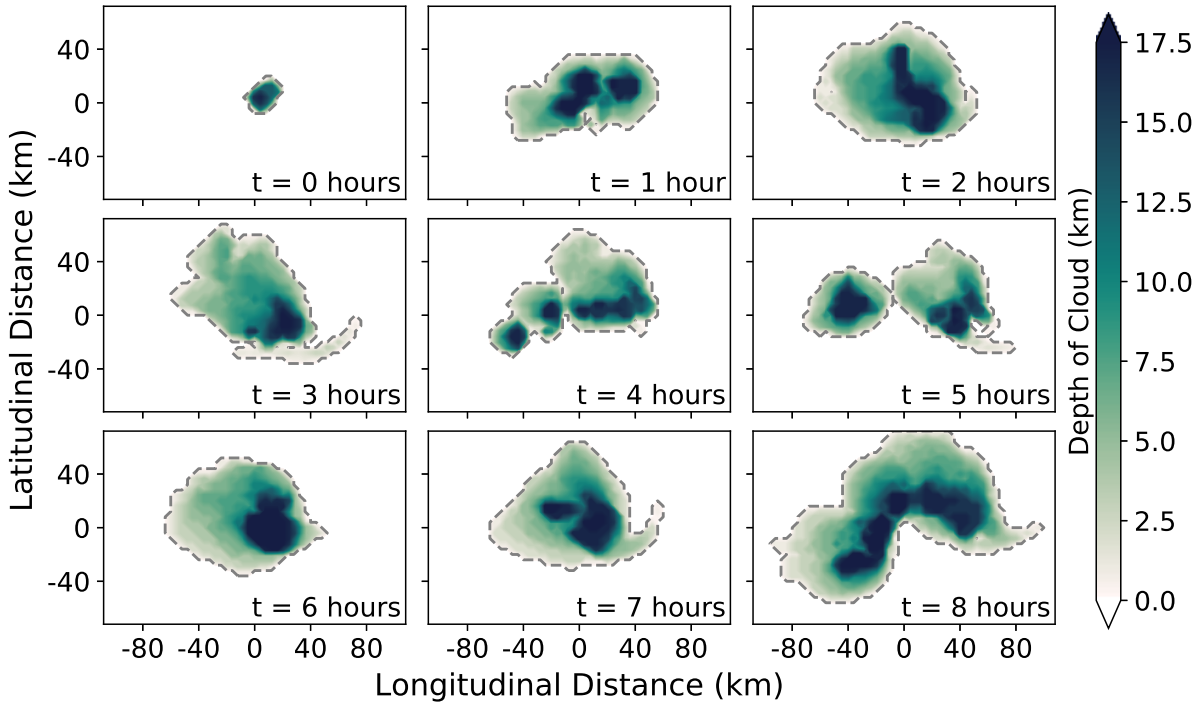

Figure 2.8: Example convective cell that was identified and tracked by the convective cell tracking algorithm. Each frame depicts an hour of convective evolution. The convective cell is centered about its centroid for each time for the purposes of this visualization, although it is not stationary within the simulation. The lateral extent of the cloud is demarcated by the gray dashed line.

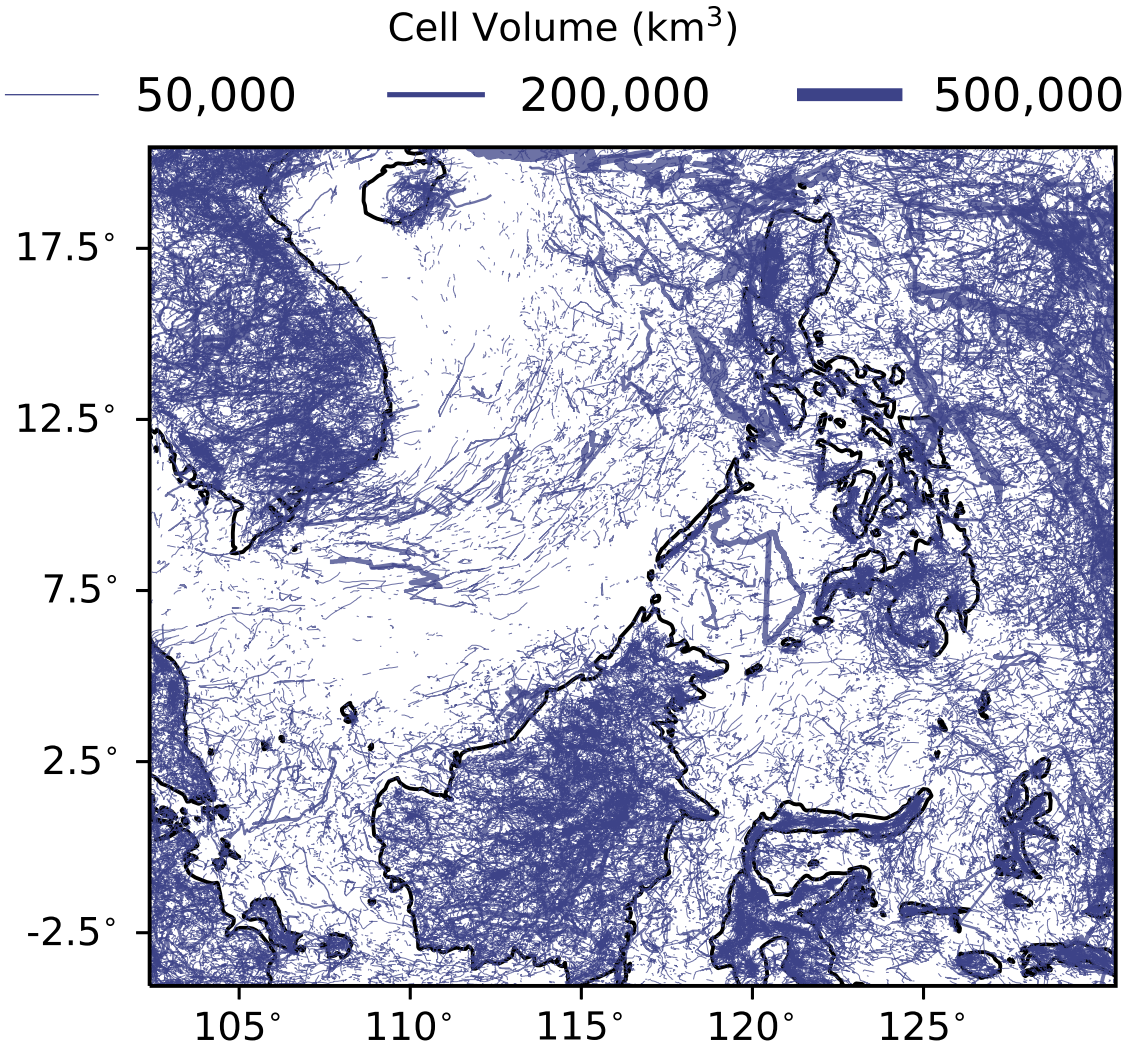

Figure 2.9: Tracks for all convective events identified within the simulation, showing the centroid of the convective cells at ten-minute intervals. The width of the tracks signifies the maximum volume of the respective convective cell throughout its lifetime. The twenty-five grid points closest to the lateral boundaries were omitted from the tracking algorithm to limit effects of the lateral boundary nudging conditions on the analysis. A total of 180,000 tracks are plotted.

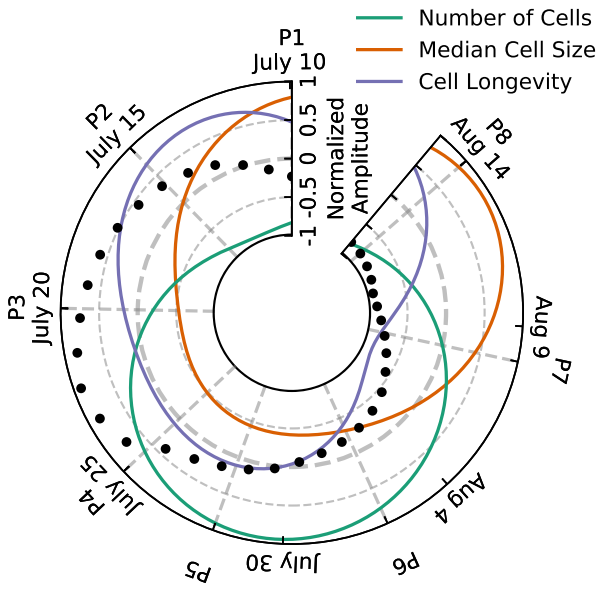

Figure 2.10: Radial time series of low-frequency (>20 day) variability in the number of convective cells (green), cell volume (orange), and cell longevity (purple) for the convectively enhanced (left) and suppressed (right) regions of the MJO, as defined by the Outgoing Longwave Radiation MJO Index (OMI). The black dots denote fraction of the domain within the respective anomalous region, a normalized amplitude of -1 corresponding to zero percent of the domain and a normalize amplitude of 1 corresponding to the entire domain. The following normalization factors were used to plot all variables on the same y-axis: cell number, 150; cell volume, 6000 km^3; cell longevity, 60 minutes.

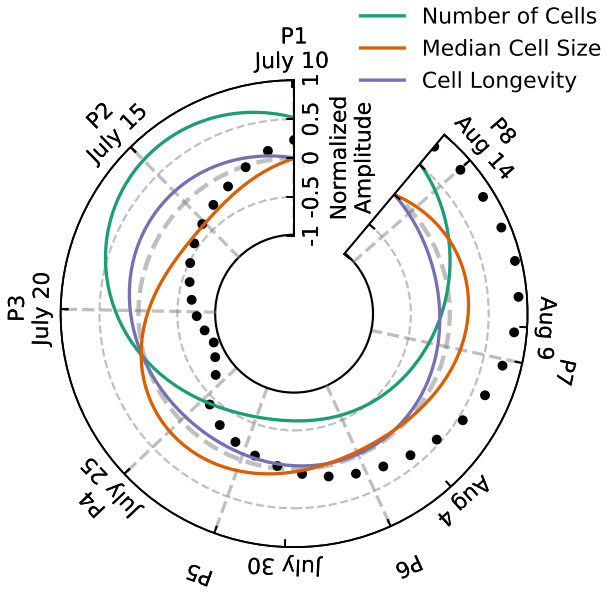

Figure 2.11: As in Figure 2.10, but for the convectively suppressed region of the MJO.

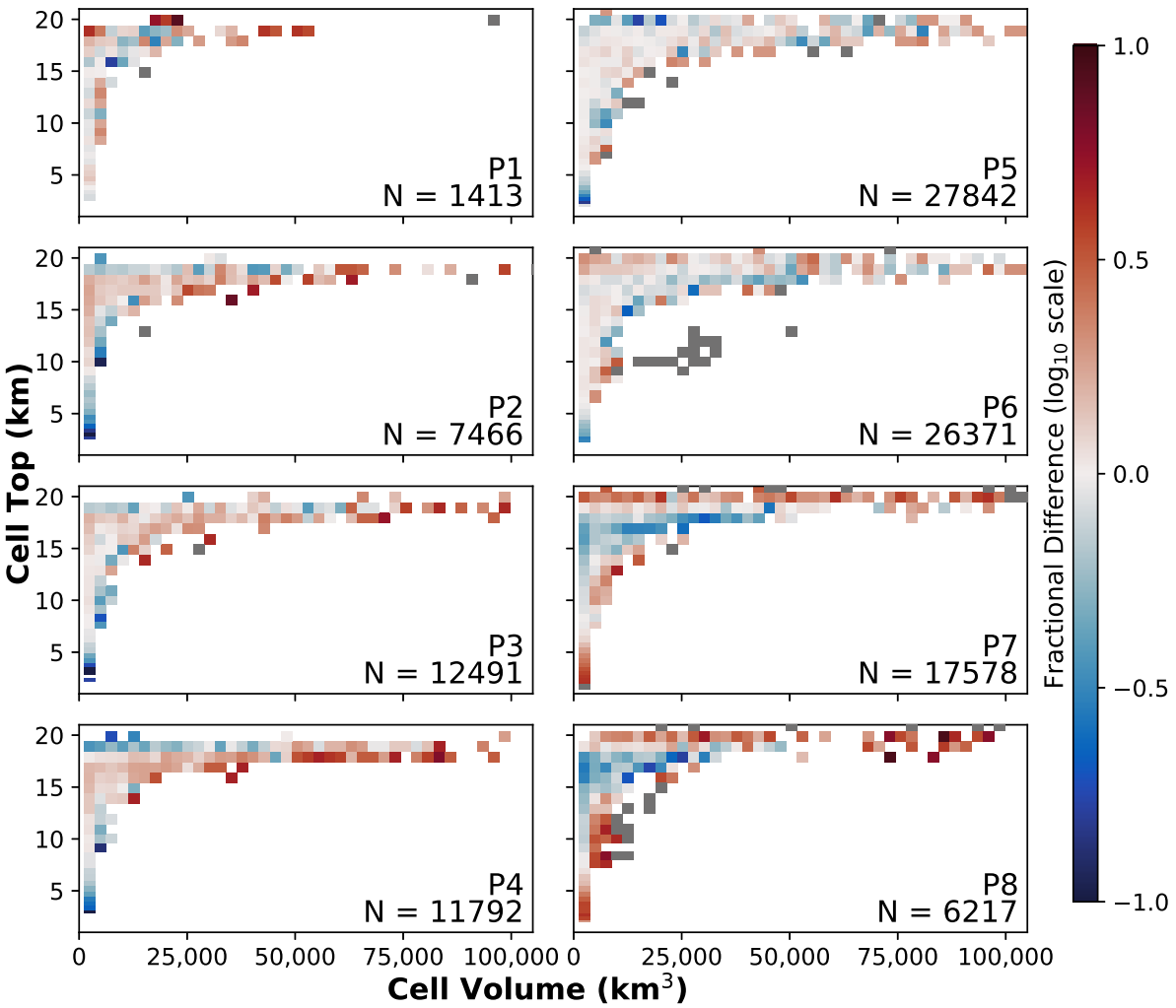

Figure 2.12: Two-dimensional histograms of cell top (y-axis) and cell volume (x-axis) for active regions within each phase of the MJO. Regions that are included within the convectively active portion of the MJO are defined as regions with negative OLR anomalies, as shown in Figure 2.3. The histograms show the anomalous fractional occurrence for each bin relative to the histogram for the entire domain and entire simulation. Red regions denote an increase in occurrences in the respective phase relative to the simulation mean, while blue regions denote a relative decrease. Gray patches indicate regions where all cases are attributed to a single phase. The number of convective cells included in each phase is listed in the bottom right corner of each histogram.

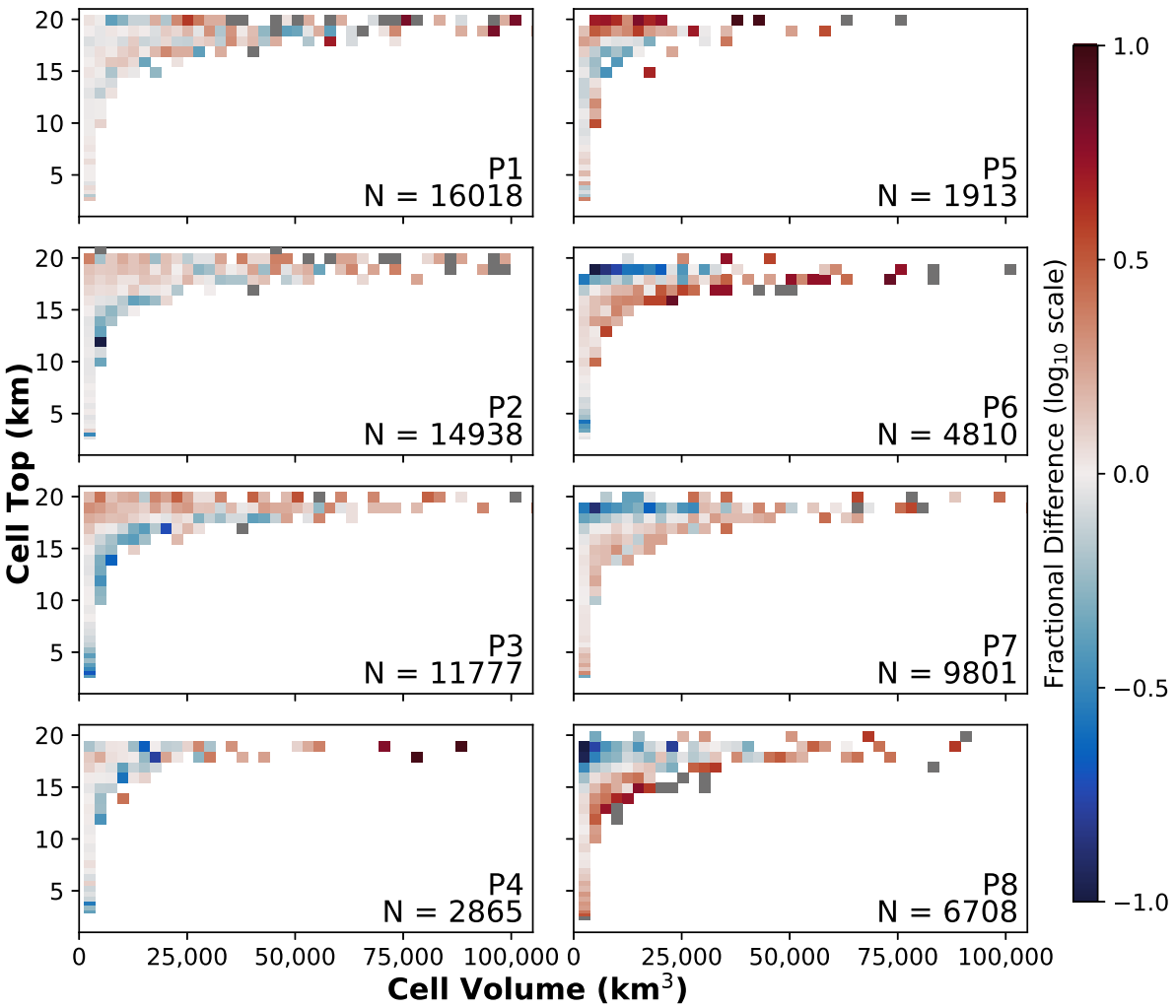

Figure 2.13: As in Figure 2.12 but for the convectively suppressed region of the MJO.

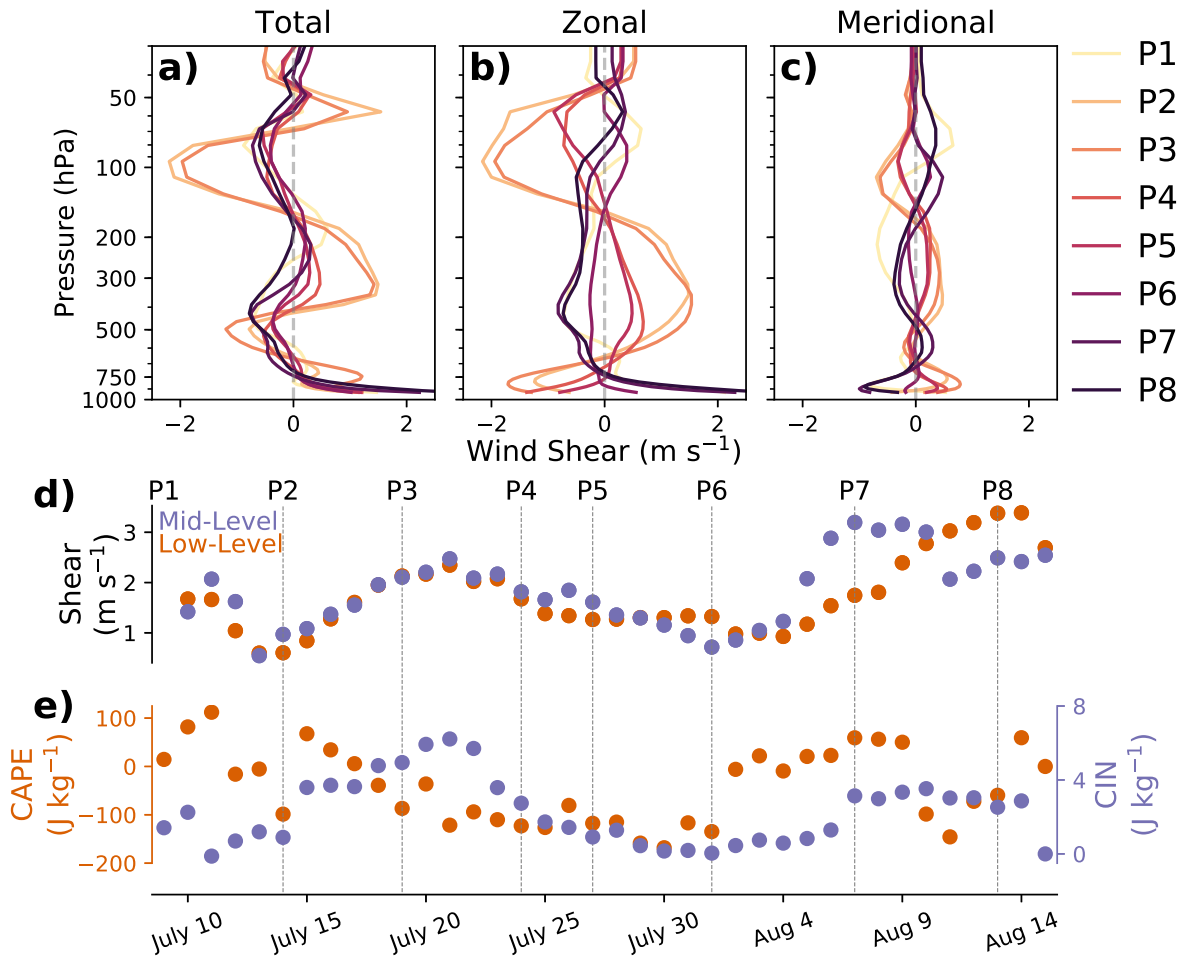

Figure 2.14: Low-frequency (> 20 day) anomalies in the atmospheric state at convective initiation within the convectively enhanced lobe of the BSISO for (a) total wind shear, (b) zonal wind shear, (c) meridional wind shear, (d) low- and mid-level shear, and (e) CAPE and CIN. Low- and mid-level shear are defined as the shear magnitude from 1000 mb to 800 mb and 800 mb to 400 mb, respectively. The shear profiles in (a), (b), and (c) are composited by MJO phase, while (d) and (e) are composited by day. Refer to the text in Section 2.6 for further details regarding how these values are calculated.

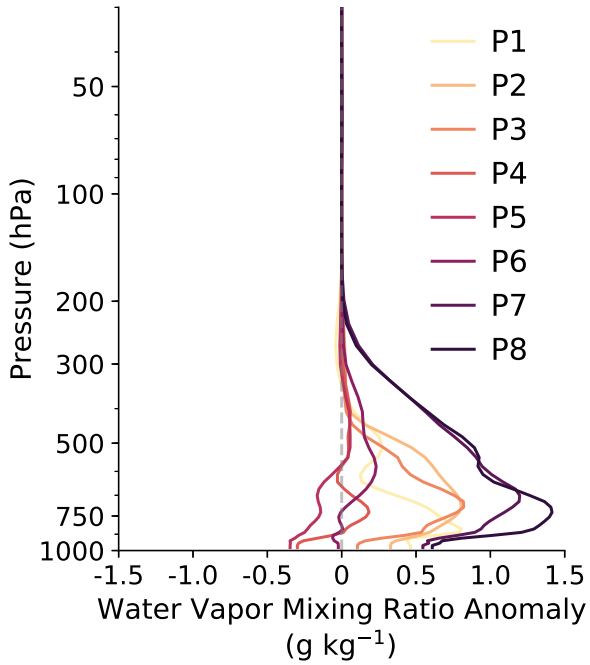

Figure 2.15: Intraseasonal ($>$ 20 day) anomalies in water vapor mixing ratio at convective initiation within the convectively enhanced lobe of the MJO for each MJO phase. Refer to the text in Section 2.6 for further details regarding how these values are calculated.

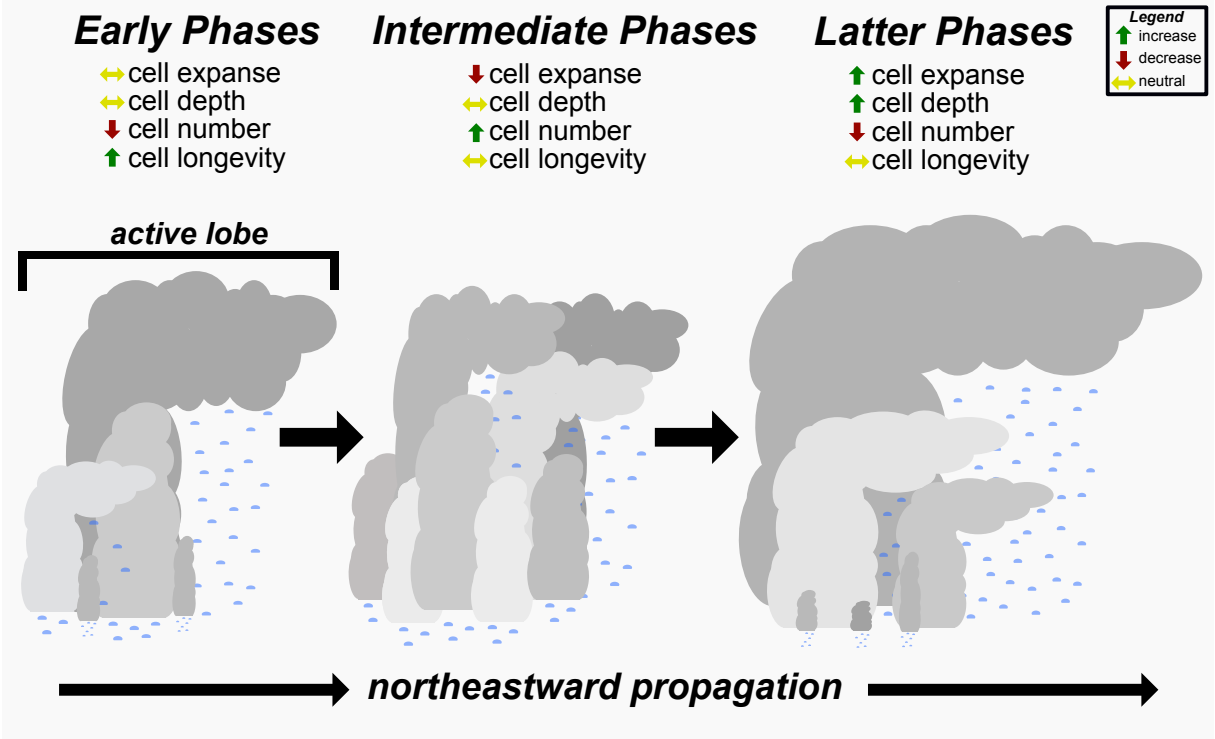

Figure 2.16: Schematic depicting the intraseasonal character of convective morphology within the convectively active region of the MJO. This schematic summarizes the findings detailed in Section 2.5. The rain drops do not have physical meaning aside from indicating that only precipitating convective clouds were included within the analysis.

Chapter 3

The Global Signature of the Madden-Julian Oscillation and its Modulation by the Quasi-Biennial Oscillation

3.1 Introduction

While mainly defined as a tropical disturbance, the Madden-Julian Oscillation (MJO; Madden and Julian (1971, 1972, 1994); Zhang (2005)) impacts the global atmosphere through teleconnections. Its tropical form is manifested through a convective anomaly that originates within the tropical western Indian Ocean and propagates across the Indo-Pacific warm pool and into the Central Pacific (Hendon and Liebmann 1994c; Kemball-Cook and Weare 2001; Powell and Houze 2013). The convective anomaly interacts with and excites other atmospheric waves across a broad range of scales, including equatorially circumnavigating Kelvin waves (Haertel et al. 2015; Powell 2017) and mixed-Rossby gravity waves (Bessafi and Wheeler 2006). Rossby gyres flank its convective response, extending into the subtropics (Kiladis et al. 2005). Further Rossby waves emanate poleward from the convective response within the Indo-Pacific warm pool, generating a Rossby wave train across the northern Pacific and into North America (Henderson et al. 2016b; Seo and Lee 2017). Additional mid-latitude linkages have been documented in the Southern Hemisphere, wherein the rainfall of Australia, subtropical South America, and Africa can be modulated by the MJO (Alvarez et al. 2017; Pohl et al. 2007; Wheeler et al. 2009). The atmosphere responds to the MJO globally, across a broad range of spatial and temporal scales.

The Quasi-Biennial Oscillation is another periodic tropical phenomenon and takes the form of a reversal in zonal wind anomalies within the lower tropical stratosphere approximately every 28 months (Baldwin et al. 2001). The QBO is driven by the depositing of easterly and westerly momentum into the stratosphere by an amalgamation of tropical waves ranging from convectively

generated inertial gravity waves on the scale of tens to hundreds of kilometers to Kelvin waves with scales of thousands of kilometers (Kawatani et al. 2010; Lindzen and Holton 1968). The QBO modulates the vertical propagation of planetary scale waves (Yang et al. 2012), which can also modulate the development of the lower-stratospheric polar vortex (Baldwin and Dunkerton 1998), which further cascades into a range of tropospheric extratropical responses (Boer and Hamilton 2008; Folland et al. 2012; Thompson et al. 2002). The global prevalence of such extratropical linkages to the QBO have been thoroughly investigated over the past decades, and recent research suggests that both the tropical and extratropical responses to the MJO may depend upon the state of the QBO.

Numerous linkages have been identified between the MJO and QBO during boreal wintertime. The seasonal average amplitude of the tropical top-of-atmosphere longwave radiative response to the MJO is approximately doubled during easterly QBO states relative to westerly QBO states (Son et al. 2017; Zhang and Zhang 2018). This increase in boreal wintertime MJO activity is caused by a greater number and increased longevity of MJO events during easterly QBO phases, rather than an increase in MJO amplitude (Hendon and Abhik 2018; Zhang and Zhang 2018). Furthermore, linkages between the MJO and the North Pacific storm track are modulated by the QBO, with easterly QBO phases favoring a more longitudinally expansive and intense storm track (Wand et al. 2018). It has thus become apparent that the QBO modulates both the tropical and extratropical characteristics of the MJO.

However, a study that quantifies the modulation of the global impacts of the MJO by the QBO does not yet exist to our knowledge. Such an analysis requires a methodology that is consistent across all latitudes, optimally utilizes the limited sample sizes available for a QBO-dependent analysis of the MJO, and maintains information regarding the wave-like nature of the MJO and its responses within the extratropics. Cross-spectral analysis considers the magnitude and phase relationships between two time series, both of which are important characteristics of waves and thereby also of tropical-extratropical interactions. Cross-spectral analysis is oftentimes a more effective method for extracting relationships at specific wave frequencies between two time series

than linear correlation, since cross-spectral analysis considers the relationship between the time series according to each harmonic mode of the time series. This enables the isolation of relationships across specific frequency bands. The advantages of cross-spectral analysis compared to linear correlation for analyses concerned with specific frequency bands is discussed further in the methods section.

We quantify the relationship between the Madden-Julian Oscillation and 300-mb geopotential variability across the globe for all seasons and QBO states using cross-spectral analysis. We first discuss the indices we use for the MJO and its global influence, and then provide a brief background on cross-spectral analysis as is relevant for this work. The dependence of the tropical and extratropical responses to the MJO on the state of the QBO is then detailed using global cross sections of the Coh^2 between the 300-mb geopotential and the MJO. We conclude by quantifying the fraction of intraseasonal 300-mb geopotential variability that can be linked to the MJO from a hemispheric and global perspective, which provides context for the prevalence of the MJO in the overall climate system.

3.2 Data and Methods

3.2.1 Definition of the MJO, QBO, and teleconnections

The tropical character of the MJO has been defined according to numerous indices, including those based solely on its convective character (Kiladis et al. 2014), its circulation patterns (Ventrice et al. 2013), and a combination of both its convective and circulation properties (Wheeler and Hendon 2004). The MJO exhibits seasonality in both its convective and circulation patterns, and numerous indices have therefore also separated the MJO into two or more seasonal modes of variability. Kikuchi et al. (2012b) developed a robust seasonal index for the MJO by separating their index into distinct boreal summertime and wintertime modes. Kiladis et al. (2014) expanded upon the premise of a bi-modal MJO by considering the evolution of the MJO on a sliding temporal window centered on each day throughout the year. Their index, dubbed the Outgoing Longwave Radiation MJO Index (OMI), is based on principal component analysis of Outgoing Longwave

Radiation (OLR) between 20S and 20N for a sliding window of 121 days, centered on each day throughout the year. Prior to performing principal component analysis, the OLR time series were filtered to include only eastward propagating signals with periods of 20 to 96 days, thereby isolating the low-frequency, eastward propagating convective response of the MJO. Some MJO indices are occasionally influenced by other convectively coupled waves (Roundy et al. 2009), but OMI is relatively immune from this issue given the particular filtering method of Kiladis et al. (2014). Most convectively coupled Kelvin waves oscillate with periods of less than 20 days, which precludes their inclusion within the principal component time series of OMI. Furthermore, according to OMI the spatial pattern of the MJO is fairly consistent during boreal wintertime and summertime, with the equinoctial seasons representing transition periods between the two otherwise predominant solstitial modes. We therefore use OMI to define the state of the MJO given its capability of capturing the state of the MJO within both the equinoctial and solstitial seasons.

Global circulation anomalies, or teleconnections, associated with the MJO have previously been identified via geopotential anomalies in the middle and upper troposphere. Anomalies in 250-mb geopotential have been used to identify teleconnections in the both the north and south Pacific (Alvarez et al. 2017; Henderson et al. 2016b), while clusters of 500-mb geopotential anomalies have been used to isolate teleconnections over North America (Riddle et al. 2013). The fact that extratropical responses to the MJO are captured well using both mid- and upper-tropospheric geopotential anomalies suggests that these anomalies are likely associated with equivalently barotropic Rossby waves. Linear waves, of which Rossby waves are a type, are supported more favorably in the upper troposphere compared to the lower stratosphere (Hoskins and Karoly 1981), which suggests that the extratropical responses to the MJO would be maximized within the upper troposphere. Furthermore, within the tropics, the amplitude of Kelvin waves is maximized at the tropopause (Randel and Wu 2005), and any of the equatorial structure of the MJO associated with Kelvin waves would therefore also likely be captured by upper-tropospheric or lower-stratospheric geopotential anomalies. We therefore use 300-mb geopotential to identify the global signature of

the MJO, although the results are generally consistent across the 500-mb through 200-mb pressure range (not shown).

Zonal wind anomalies associated with the QBO are most pronounced within the lower to middle stratosphere, generally spanning from approximately 70 mb to 10 mb (Naujokat 1986). The state of the QBO is commonly defined according to 30-mb or 50-mb zonal wind anomalies since these pressure levels capture the core of the QBO (Holton and Tan 1980; Pascoe et al. 2005). We define the QBO based on 50-mb zonal wind anomalies, although sensitivity tests suggest that the results are similar when using the 30-mb zonal wind anomalies (not shown).

The global response to the MJO is quantified via the magnitude-squared coherence between time series of 300-mb geopotential anomalies at each grid box within reanalysis and the two OMI principal components from 1980 through 2016, divided into season and QBO phase. We use daily 300-mb geopotential data from ERA-Interim (Dee et al. 2011), which renders a grid spacing of $\sim$ 60 km at the equator and $\sim$ 30 km at 60°N/S, with grid size further decreasing toward the poles (Dee et al. 2011). Anomalies in 300-mb geopotential are then calculated independently for each grid point within ERA-Interim by subtracting the 1980 through 2016 mean, linear trend, and seasonal cycle for each respective grid point. We define the seasonal cycle for each grid point as the first three harmonics of the mean daily annual cycle from 1980 through 2016.

The four meteorological seasons are considered independently, divided into December/January/February (DJF), March/April/May (MAM), June/July/August (JJA), and September/October/November (SON) as boreal winter, spring, summer, and fall, respectively. Each season is defined as a 96 day period since OMI defines the MJO with a period of 20 to 96 days, and the 96-day season therefore permits the consideration of the maximum longevity of an individual MJO event within each season. Except for the QBO-blind analyses which include all years from 1980 through 2016, only seasons during which the average magnitude of zonal wind anomalies at 50-mb was greater than 0.5-σ (σ = 7.27 m s^{-1}) are considered to ensure that the QBO signal was strong during the analysis periods. Figure 3.1 presents all such seasons that satisfy this QBO-magnitude criterion for the 1980 to 2016 period.

3.2.2 Cross-Spectral Analysis

Cross-spectra are a representation of the co-variability between the Fourier modes of two signals, and therefore serve as a robust tool for quantifying the relationship between two periodic time series. Below, we briefly introduce the mathematical formulation of cross-spectral analysis and one of its derivatives, magnitude-squared coherence, which we use throughout the remainder of the paper.

Two time series x and y can be represented by their complex exponential Fourier expansions as

$$x(t) = \overline{x} + \frac{1}{2}\sum_{-\frac{N}{2}}^{\frac{N}{2}}(A_{xk} - iB_{xk})e^{i\left(\frac{2\pi kt}{T}\right)} = \overline{x} + \sum_{-\frac{N}{2}}^{\frac{N}{2}}F_x(k) \tag{3.1}$$

$$y(t) = \overline{y} + \frac{1}{2}\sum_{-\frac{N}{2}}^{\frac{N}{2}}(A_{yk} - iB_{yk})e^{i\left(\frac{2\pi kt}{T}\right)} = \overline{y} + \sum_{-\frac{N}{2}}^{\frac{N}{2}}F_y(k) \tag{3.2}$$

where A and B are the cosine and sine Fourier coefficients, t is time, T is the length of the record, $F(k)$ is the complex Fourier series as a function of wave number k, and the summation is performed across the positive and negative $\frac{N}{2}$ Fourier modes. The cross-spectrum of x and y can be calculated by combining their complex Fourier series as:

$$F_x(k)F_y^*(k) = \frac{1}{4}(A_{xk} - iB_{xk})e^{i\left(\frac{2\pi kt}{T}\right)}(A_{yk} - iB_{yk})e^{i\left(\frac{2\pi kt}{T}\right)} \tag{3.3}$$

$$= \frac{1}{4}\{A_{xk}A_{yk} + B_{xk}B_{yk} + i(A_{xk}B_{yk} - A_{yk}B_{xk})\} \tag{3.4}$$

where $F_x(k)F_y^*(k)$, hereafter F_{xy}, is the complex cross spectrum and A and B are as previously defined for the Fourier expansions of x and y. Note that the complex cross spectrum can be separated into its real and imaginary parts – the real portion is the co-spectrum and the imaginary portion is the quadrature spectrum:

$$Co - spectrum = CO(k) = A_{xk}A_{yk} + B_{xk}B_{yk} \tag{3.5}$$

$$Quadrature\ spectrum = Q(k) = A_{xk}B_{yk} - A_{yk}B_{xk} \tag{3.6}$$

The co-spectrum represents the in-phase portion of x and y for each Fourier mode, while the quadrature spectrum represents the out of phase portion of x and y. Conceptually, the co-spectrum is the linear covariance between x and y as a function of wavenumber k. Since the complex cross spectrum is a function of wave number k, it can be segmented into bands of wave numbers and interpreted as the co-variability between x and y across a range of k.

The decomposition of the complex cross spectrum can be taken a step further to calculate the magnitude-squared coherence ($Coh^2(k)$) between the two signals. The magnitude-squared coherence between two signals is defined as

$$Coh(k)^2 = \frac{|F_{xy}(k)|^2}{F_{xx}(k)F_{yy}(k)} \tag{3.7}$$

where $|F_{xy}(k)|$ is the magnitude of the complex co-spectrum of x and y as previously defined in Equation 3.4 and $F_{xx}(k)$ and $F_{yy}(k)$ are their individual power spectra. $Coh^2(k)$ is typically calculated from an average of cross spectra from multiple samples of two time series, in which case $|F_{xy}(k)|$, $F_{xx}(k)$, and $F_{yy}(k)$ represent the cross spectra and power spectra of x and y averaged across a number of samples. $Coh^2(k)$ is thereby a metric for the consistency of the amplitude and phase relationships between two signals across numerous samples; the Coh^2 is reduced when the amplitude and phase relationships vary across samples and is maximized when they are similar. $Coh^2(k)$ ranges from 0 to 1, where 0 corresponds to the case where no magnitude or phase relationships exist at wave number k and 1 corresponds to the case where the signals of x and y are identical at wave number k across all samples. As previously mentioned, it can be linearly separated into its Fourier modes, which allows for the interpretation of relationships between two time series for specific frequency bands. *Coh^2 can be interpreted as the fraction of signal y that can be explained by variability in signal x at a particular frequency or across a frequency band.* Furthermore, since Coh^2 is calculated across multiple samples and is an estimate of the similarities in the relationship between x and y across each sample, it is a metric for the *coherence* of

the relationship between two signals, rather than the magnitude. Throughout the remainder of this paper, we will therefore refer to the Coh^2 between two time series as an estimate of the coherence of their magnitude and phase relationships.

Of note, Coh^2 can be a more effective metric for estimating the relationship between two periodic signals than linear correlation, especially if the analysis is concerned with a relationship across a specific band of wave frequencies. Matthews et al. (2006) used linear correlation to quantify the relationship between the MJO and Northern Hemispheric extratropical circulation patterns, although we approach the problem using Coh^2, which is effective at both considering phase shifts between two time series and isolating relationships within specific frequency bands. Coh^2 therefore captures the relationship between two periodic signals at specific frequency bands, something standard linear correlation cannot do. Figure 3.2 provides various examples of periodic signals and their associated Coh^2 and linear correlation values. As can be seen for the most basic comparison between two signals with similar amplitude and frequency but shifted phase, the linear correlation decreases toward zero at a phase shift of 180 degrees. However, consider the case wherein the two phase-shifted signals are indeed related to one another, with one signal simply preceding the other. In this case, the relationship between the two time series perceived from linear correlation changes depending on the phase shift, whereas the Coh^2 is always unity. Another plausible scenario exists wherein the periodic signal within y that is related to x is convoluted by another coincident signal, z, with different wave characteristics (Figure 3.2(e,f)). In this scenario, the linear correlation between x and y is reduced by the coincident signal z, but the Coh^2 between x and y at the period at which x oscillates is, again, unity. These distinctions between linear correlation and Coh^2 are critical for periodic atmospheric phenomena such as teleconnections that are driven by the MJO, which are typically phase-shifted from the tropical signal of the MJO and convoluted by coincident atmospheric patterns (Henderson et al. 2017; Stan et al. 2017).

3.2.3 Application of Cross-Spectral Analysis to the Global Response of the MJO

We isolate the global signature of the MJO using magnitude-squared coherence (Coh^2). The subsequent analyses consider disturbances with periods within the 20 to 96 day band since OMI was constructed using outgoing longwave radiation anomalies within this band. The majority of the variability of the OMI principal components exists with periods of 20 to 96 days, although approximately one percent of variability within the principal components of OMI does exist outside of this band within the 96 to 120 day band (Figure 3.3). Since each season is defined as a 96 day period, the analyses consider atmospheric variability with periods of up to 96 days and therefore consider the intraseasonal influences of the MJO.

We quantify the periodic relationship between the MJO and 300-mb geopotential anomalies according to the following procedure, which is completed for every grid cell at 300 mb within ERA-Interim. First, the Coh^2 is calculated between PC1 and PC2 of OMI and time-series of 300-mb geopotential at every location across the globe, separately for PC1 and PC2. The Coh^2 is then averaged across the 20 to 96 day band, which results in a 20 to 96 day mean Coh^2 between OMI and 300-mb geopotential. Then, we estimate the variance of 300-mb geopotential that is linked to the MJO at every location across the globe. To do so, the power spectra for 300-mb geopotential are calculated at each grid cell based on the 1980 through 2017 period, and the Coh^2 between the two OMI principal components and 300-mb geopotential is then multiplied linearly to the power spectra and summed across the 20-to-96 day band. This process is conceptually similar to estimating the fraction of variability in 300-mb geopotential associated with the MJO by multiplying the variance in 300-mb geopotential by the squared correlation between OMI and 300-mb geopotential, although, as previously discussed, we use Coh^2 since it better captures the covariability between two periodic signals. By normalizing the amount of variability in 300-mb geopotential linked to the MJO by the total amount of variability in 300-mb geopotential, we further estimate the fraction of 300-mb geopotential variability that is linked to the MJO across all timescales.

It is important to note that OMI PC1 and PC2 do not necessarily carry unique information. When linearly combined, PC1 and PC2 represent the progression of an MJO event through its lifecycle, and thereby a change in PC1 might be similarly represented by a change in PC2. OMI was constructed so as to reduce the impacts of other convectively coupled waves on its principal components (Kiladis et al. 2014). Any unique information within each principal component time series is therefore likely associated with the MJO, and not another form of convectively coupled wave. We therefore estimate the fraction of PC2 that is truly unique from PC1 by calculating the Coh^2 between time series of each principal component for the years 1980 through 2016 averaged across the 20 to 96 day band, which results in a Coh^2 of 0.685. This implies that approximately 31.5% of the PC2 time series is unique from PC1, and we therefore scale the average Coh^2 between OMI PC1 and PC2 and 300-mb geopotential by a factor of $\frac{1}{0.685} = 1.46$ to estimate the total variance explained by the MJO from both PC1 and PC2, that is, $Coh^2_{total} = 1.46(0.5Coh^2_{PC1} + 0.5Coh^2_{PC2})$.

Of note, the El Niño-Southern Oscillation (ENSO; Ashok et al. (2007); Diaz et al. (2001); Yu and Kim (2013)) occurs on similar timescales to the QBO and has been shown to occasionally be modulated by the MJO (Slingo et al. 1999a; Zhang and Gottschalck 2002), and is therefore a potential source of interference in analyses of the relationships between the MJO and the QBO. We therefore tested the dependence of the analysis on ENSO using two methods. For the first method, the ENSO teleconnection pattern was removed from the 300-mb geopotential field by regressing a smoothed daily Oceanic Niño Index (ONI) time series spanning from 1980 through 2016 onto the 300-mb geopotential field across a similar time span. The presented results include this method of removing the ENSO teleconnection pattern. For the second method, we completed the same analysis as described earlier within this section, but beforehand we removed all seasons during which a significant ENSO event occurred, which for ONI is defined as a 3-month long average of sea-surface temperature anomalies of greater or less than 0.5 degrees Celsius. This method substantially reduces the number of samples and thereby introduces problems with statistical significance. However, the spatial pattern of teleconnections for this more direct method of removing

the ENSO signal are similar to that of the regression method, which lends confidence that the ENSO signal does not substantially alter the dependence of MJO teleconnection patterns on the phase of the QBO (not shown).

Statistical Significance

We use a Monte Carlo approach to estimate bounds of statistical significance. The lag-one autocorrelation of 300-mb geopotential is calculated for each grid cell across the globe for all seasons and both the QBO-ignorant and easterly and westerly QBO phases. For each grid cell, the autocorrelation is then used to generate 10,000 realizations of red noise. The Coh^2 between the 10,000 red noise realizations and the OMI principal component time series, split into the QBO-ignorant, westerly QBO, and easterly QBO time periods, is then calculated for each location. This method generates distribution of possible Coh^2 values for each season and QBO phase, from which the 95th percentile bound is calculated. These bounds represent the 95th percentile confidence bounds that the Coh^2 values for each season and QBO phase are differentiable from red noise. We also estimate the statistical significance of the difference between the MJO-linked 300-mb geopotential variability during easterly and westerly QBO phases using a similar Monte Carlo approach. The difference between the Coh^2 values between the 10,000 red noise realizations and the OMI principal component time series for the westerly and easterly QBO phases is calculated, which generates a distribution of expected differences in the Coh^2 between the westerly and easterly QBO phases. The bounds for the difference in Coh^2 between the two QBO phases are then estimated by finding the 5th and 95th percentile thresholds of these distributions. The 5th and 95th percentile bounds thereby represent the two-tailed 90th percentile confidence bounds that the difference in Coh^2 between the easterly and westerly QBO states is differentiable from red noise.

After completing this process, we find that the lag-one auto-correlation, or redness of the time series, for each location does not strongly influence the Coh^2 between the red noise realizations and OMI PC1/PC2 (data not shown). Rather, the season and QBO phase control the distribution of possible Coh^2 values between the red noise realizations and OMI PC1/PC2, and we therefore approximate the 5th and 95th percentile confidence bounds to be the same for every location across

the globe and to depend only upon season and QBO state. This is not an assumption that 300-mb geopotential anomalies behave as white noise, but rather a simplification resulting from the redness of the time series of 300-mb geopotential not substantially influencing the estimated bounds of the Coh^2 differences between the easterly and westerly QBO phases. The calculated confidence bounds are listed in Table 3.1.

3.3 Global Signature of the MJO

3.3.1 Coherence-Based Analysis

We first determine the locations of coherent signals in 300-mb geopotential anomalies associated with the MJO, then quantify the prevalence of the MJO within the overall climate system by calculating the mean latitudinal, hemispheric, and global distributions of 300-mb geopotential anomalies that are associated with the MJO. The subsequent analysis quantifies the tropical and extratropical signature of the MJO and provides a lower bound on the prevalence of the MJO within Earth's climate system.

QBO-Blind Response

We use the Coh^2 between the two principal components of OMI and 300-mb geopotential anomalies to estimate the location and magnitude of MJO linkages across the globe for all seasons (Figure 3.4). As discussed in Section 3.2.2, since Coh^2 is an estimate of the fraction of variability in two time series that can be mutually explained by each other, the Coh^2 between the OMI principal components and 300-mb geopotential anomalies represents the fraction of variability in 300-mb geopotential anomalies that is associated with the MJO.

Numerous papers have investigated the global response to MJO-like forcing within the tropics using global circulation models and linear, idealized models, which provides an opportunity to validate the location of a subset of the teleconnections depicted in Figure 3.4. The extratropical response to the MJO identified using our methods is similar to these previous studies in both spatial expanse and magnitude, particularly within the northern Pacific and North American regions.

Henderson et al. (2017) identified a PNA-like pattern that emanates from the Indo-Pacific region throughout the northern Pacific and into North America that results from convective heating resemblant of the MJO over the Indo-Pacific during boreal wintertime. This signal is also captured within our analysis (Figure 3.4(a)), wherein the the regions of high Coh^2 align with the centers of the geopotential anomalies identified by Henderson et al. (2017). This consistency increases confidence that the cross-spectral analysis methods capture patterns that would also be identified by process-oriented studies. The southern hemispheric response to the MJO has been shown to be similar to the PNA-like pattern observed within the Northern Hemisphere, with a teleconnection pattern emanating poleward and eastward from the Indo-Pacific region (Alvarez et al. 2016). Alvarez et al. (2016) showed this predominant teleconnection pattern to be the most prominent during austral winter (JJA) and spring (SON), which is also apparent within the Coh^2-based analysis. However, contrary to Alvarez et al. (2016), the Coh^2-based analysis suggests that the austral summertime (JJA) teleconnections within the southern hemisphere are not statistically significant beyond the 90^{th} percentile, which suggests that the teleconnection locations and/or amplitudes are inconsistent across the 1980 through 2017 period. This difference between the compositing-based methods of Alvarez et al. (2016) and the Coh^2-based methods presented herein highlights the capabilities of the Coh^2-based analysis in isolating the teleconnections with the most consistent characteristics across the years, which limits teleconnections that occur in only a limited number of samples from dominating the statistical signal.

The extratropical linkages to the MJO are most prominent during the wintertime of the respective hemispheres (Figure 3.4(a,c)). This tropical-extratropical coupling is likely associated with the more prominent circumglobal waveguide present during the wintertime of each hemisphere, which encourages the maintenance and propagation of extratropical circulation responses to tropical convective heating (Yuan et al. 2011). Specifically, a teleconnection pattern appears to emanate from the Indo-Pacific region, northward during boreal wintertime and southward during boreal summertime, extending from approximately 120°E to 140°W. This emanation from the Indo-Pacific is more consistent during boreal wintertime than boreal summertime. During boreal

summertime, two lobes of subtropical anomalies exist off the western coasts of the Americas. Additional extratropical linkages do still exist during hemispheric summertime, although they are generally constrained to the subtropics and tend to be less coherent than those during hemispheric wintertime. The circulation response to the MJO is markedly less coherent during fall and spring for each hemisphere, although the extratropical responses during the winter and spring of each respective hemisphere do tend to be similar (Figure 3.4(b,d)).

Beyond the extratropical signature of the MJO, the tropical signature differs from the expectations set forth by prior research. It is well cited in the literature that the MJO is most equatorially active during the boreal wintertime, with off-equatorial propagation and a generally weaker signal during boreal summertime (Kiladis et al. 2014; Wheeler and Hendon 2004). However, according to OMI, the 300-mb geopotential response to the MJO within the tropics is both substantially more coherent and zonally homogeneous during boreal summertime compared to boreal wintertime (Figure 3.4(a,c)). During boreal wintertime, no coherent signal exists between the MJO and 300-mb geopotential anomalies over the central Pacific or Atlantic oceans, with is starkly contrasted by the persistent band of high Coh^2 across the entirety of the tropics during boreal summertime. Furthermore, the amount of 300-mb geopotential variance within the tropics is greater during boreal summertime compared to during boreal wintertime, which suggests that the increased coherence between the MJO and upper-tropospheric geopotential anomalies is also associated with an increase in the total variance of tropical 300-mb geopotential (further discussed in Section 3.3.1).

QBO-Dependent Response

The Coh^2-based analysis was also completed for all seasons for both easterly and westerly QBO phases. Only seasons during which the average magnitude of zonal wind anomalies at 50-mb was greater than 0.5-σ (σ = 7.27 m s^{-1}) were considered to ensure that the QBO signal was strong during the analysis periods (Figure 3.1). Summarily, both the locations and coherence of linkages between 300-mb geopotential anomalies and the MJO strongly depend on the phase of the QBO (Figures 3.5 through 3.7). The most stark contrast occurs during boreal wintertime, during which the equatorial signature of the MJO is substantially magnified during easterly QBO phases relative

to westerly QBO phases. The enhancement of the tropical MJO signal during easterly QBO phases is consistent with previous research that has shown the the MJO to be more persistent and recur more frequently during easterly QBO states (Zhang and Zhang 2018). During boreal wintertime of westerly QBO states, tropical upper tropospheric geopotential anomalies are incoherent across years as indicated by the lack of statistically significant Coh^2 anomalies (Figure 3.5(a)). In fact, the northern hemispheric 300-mb extratropical response is more coherent than the tropical response during boreal wintertime of westerly QBO phases.

The emanation of teleconnection patterns from the Indo-Pacific toward the polar regions of each respective hemisphere during hemispheric wintertime is less pronounced during westerly QBO phases compared to the QBO-blind analysis (Figure 3.5). That being said, the geopotential anomalies within the northern Pacific are particularly coherent during westerly QBO states. The Coh^2 within the tropics is much greater during boreal summertime than boreal wintertime, consistent with the QBO-blind analysis. It is also difficult to discern any pattern within the extatropical response to the MJO during spring and fall, during which the teleconnections are smaller in spatial extent and scattered across the globe (Figure 3.5(b,d)). The MJO undergoes a period of transition during spring and fall, during which the characteristics of the summertime and wintertime MJO intermittently ebb and flow, which may cause the more chaotic teleconnection patterns during these seasons. (Kikuchi et al. 2012b; Kiladis et al. 2014).

During easterly QBO phases, the 300-mb equatorial signature of the MJO during boreal wintertime is similarly coherent to the signature during boreal summertime, although it is less zonally homogeneous (Figure 3.6). A prominent gap exists in the Coh^2 within the eastern Pacific during boreal wintertime, whereas no such gap exists during the boreal summertime. The presence of a secondary convective maximum during boreal summertime over the eastern Pacific may drive the increased coherence within this region (Maloney and Esbensen 2003). Another explanation may relate to the favorable conditions for extratropical waves intruding upon the tropical circulation within the Eastern Pacific during boreal wintertime due to the presence of a westerly wave duct (Webster and Holton 1982). Beyond the tropics, the teleconnection pattern that emanates from the

Indo-Pacific during hemispheric wintertime is prominent during easterly QBO phases within both hemispheres. Similar to westerly QBO phases, the fall and spring teleconnection pattern is more scattered compared to the summer and winter pattern (Figure 3.6(b,d)). In addition, an Arctic teleconnection exists during boreal summertime for easterly QBO phases that does not exist during boreal summertime for westerly QBO phases (Figure 3.6(a)). It is unclear whether the increased coherence of extratropical teleconnections is driven by the more consistent tropical convective structure of the MJO during easterly QBO phases or by a more favorable extratropical waveguide.

It is worth noting that the statistical significance of teleconnections are identified by the 90th percentile confidence bounds that the coherence is distinguishable from noise, but the entire spatial extent of the teleconnections are likely not captured by this metric. Locations surrounding the regions identified by the 90th percentile threshold appear to be strongly spatially correlated with the maximas, which is related to the well-known idea that 300-mb geopotential has spatial correlation. Readers must therefore be careful when interpreting Figures 3.4 through 3.7 and should consider the regions identified by the 90th percentile confidence bounds as the maximas of teleconnections, rather than their entire spatial expanse. This analysis therefore offers an opportunity for focusing on specific teleconnections and identifying their spatial extent and variability in future process studies of circulation patterns driven by the MJO.

When directly comparing the easterly and westerly QBO phases, the most apparent difference is that the location of teleconnection patterns depends on QBO phase (Figure 3.7). The differences between the teleconnection patterns during westerly and easterly QBO phases is most apparent within the tropics and subtropics during boreal wintertime, since the coupling between the MJO and 300-mb geopotential is incoherent during boreal wintertime of westerly QBO phases relative to easterly QBO phases. The differences between the two QBO phases are less structured during boreal spring, fall, and summer, with patches of positive and negative anomalies distributed across the globe. It does appear that the magnitude of the coherence of teleconnections during easterly QBO phases is greater than that during westerly QBO phases, although this is best interpreted through latitudinal and global averages of Coh^2, which will be discussed subsequently.

When the 300-mb geopotential response to the MJO is averaged across all longitudes for each QBO state, the relationship between teleconnections associated with the MJO and QBO phase becomes more apparent (Figure 3.8). During easterly QBO phases, the global coherence of MJO teleconnections is enhanced, regardless of latitude or season. The one exception to this statement is within the polar regions, wherein a more complicated relationship between MJO linkages and QBO phase exists. During boreal summer, fall, and winter, westerly QBO events are associated with an enhancement of MJO linkages within the southern hemispheric polar regions, while easterly QBO events are associated with enhancements for all other latitudes. In the zonal mean, the coherence of tropical linkages is increased during easterly QBO phases for boreal summertime and wintertime, although not during boreal spring nor fall. The coherence of extratropical linkages is increased most substantially during easterly QBO states for boreal wintertime, although boreal fall also exhibits more consistent extratropical linkages during easterly QBO states within both the northern and southern hemispheres. The extratropical signal during boreal spring is more convoluted and difficult to interpret, while the increased coherence of extratropical signatures for boreal summertime during easterly QBO states is constrained to the southern hemispheric sub-tropics.

Hemispheric and Global Variability

We quantify the prevalence of the MJO within the global climate system by estimating the fraction of hemispheric and global variability in 300-mb geopotential on intraseasonal timescales that can be linked to the MJO. To do so, the Coh^2 between PC1 and PC2 of OMI and 300-mb geopotential anomalies at each location is multiplied by the power spectra of 300-mb geopotential anomalies independently for each harmonic frequency at each grid point. Then, this quantity is summed across the 30 to 96 day band and divided by the summed variance in the 2 to 96 day band, which can be expressed formulaically as

$$Var_{MJO} = \frac{\sum_{\tau=30\ days}^{\tau=96\ days}(Coh_{\tau}^{2})(F_{ZZ,\tau})}{\sum_{\tau=2\ days}^{\tau=96\ days} F_{ZZ,\tau}} \tag{3.8}$$

where τ denotes the period of the individual harmonic modes and F_{ZZ} is the power spectrum of 300-mb geopotential anomalies. The resultant value, Var_{MJO}, is the fraction of 2 to 96 day variance that can be linked to the 30 to 96 day MJO. Figure 3.9 shows the hemispheric, tropical, and global variance in 2 to 96 day 300-mb geopotential anomalies linked to the MJO calculated using Equation 3.8, separated into QBO state and season.

The global prevalence of 300-mb geopotential anomalies during easterly QBO phases becomes even more apparent when considering the global and hemispheric perspectives of the fraction of 300-mb geopotential variability that is associated with the MJO (Figure 3.9). Globally, during easterly QBO phases the MJO is associated with approximately 13% of all intraseasonal variability in 300-mb geopotential during boreal wintertime and only 7% percent during westerly QBO phases. The fraction of variability associated with the MJO during boreal wintertime and summertime is similar during easterly QBO phases ($\sim$11% to 12%), whereas during westerly QBO phases the variability during boreal summertime is 1.6 times greater than during boreal wintertime. It is very apparent that the QBO-blind analysis underestimates the fraction of 300-mb geopotential variability associated with the MJO. This underestimation is likely caused by the displacement of teleconnections between easterly and westerly QBO phases, as shown in Figure 3.7. By including seasons during which the teleconnection patterns are dissimilar because of the influences of the QBO, the Coh^2 is reduced because of the inconsistency in the relationship between the MJO and teleconnections across the samples. *This finding suggests that it is important to consider the state of the QBO in analyses related to the MJO, particularly for studies focusing on the coupling between the extratropics and the MJO.*

It is interesting to note that MJO-driven teleconnections within the southern hemisphere are most prevalent during southern hemispheric fall and spring. Within the northern hemisphere the teleconnections are most prevalent during winter and spring, which is consistent with the wintertime mode of the MJO being most active during these seasons (Kikuchi et al. 2012b). Regardless of season or QBO phase, the MJO explains as much or more variability within the northern hemisphere than the southern hemisphere. MJO teleconnections are nearly half as coherent within

the southern hemisphere during southern hemispheric wintertime compared to the teleconnections within the northern hemisphere during northern hemispheric wintertime, which may be related to either the convective maximum of the MJO being displaced north of the equator during the boreal summertime or differences in the nature of extratropical variability between the northern and southern hemispheres. The proximity of the waveguides associated with the jet streams to the source of convective heating is important for the maintenance and propagation of extratropical teleconnections (Stan et al. 2017; Yuan et al. 2011). While the southern hemispheric jet streams move equatorward during southern hemispheric wintertime, the convective maximum of the MJO moves northward, away from the equator. Perhaps this movement of the convective maximum of the MJO to north of the equator during austral winter prevents the convectively generated wave energetics from fully interacting with the austral winter waveguide.

3.4 Summary and Conclusions

The influence of the Madden-Julian Oscillation spans from the tropics to the poles. Although its influence extends across all latitudes of Earth, the location and magnitude of its impacts depend on the background state of the atmosphere (Hendon and Abhik 2018; Jiang et al. 2018; Slingo et al. 1999b). Recent research has suggested that the tropical and extratropical character of the MJO depends on the state of the Quasi-Biennial Oscillation (QBO), with easterly QBO phases favoring a more persistent and rapidly recurring tropical convective signal of the MJO (Lee and Klingaman 2018; Zhang and Zhang 2018). With this in mind, we analyze the global character of upper tropospheric-lower stratospheric geopotential anomalies connected with the MJO to determine any dependencies of these linkages on the state of the QBO.

We used magnitude-squared coherence (Coh^2), a derivative of cross-spectral analysis, to estimate the significance of the global teleconnections of the MJO. Coh^2 is a metric that considers both the amplitude and phase relationships between two periodic signals, and while its final form is mathematically similar to correlation, its inclusion of information regarding both the amplitude and phase can make it a more reliable proxy for quantifying the relationship between periodic

phenomena than linear correlation, especially when considering relationships across a specific frequency band (Guevara and Corsi-Cabrera 1996) (Figure 3.2). Coh^2 ranges between 0 and 1 and can be interpreted as the fraction of variability of one time series, y, that can be explained by variability of another time series, x. We thereby also quantified the fraction of 300-mb geopotential anomalies that can be linked to the MJO, first from the perspective of global cross sections of Coh^2 between 300-mb geopotential and the MJO, then by hemispheric and global integrations of the 300-mb Coh^2 cross sections.

Summarily, the location and coherence of MJO teleconnections across the globe depend on QBO phase (Figures 3.4 through 3.9). Teleconnections of 300-mb geopotential are generally more coherent and ubiquitous during easterly QBO phases, especially within the Northern Hemisphere. The extratropical signal of the MJO in 300-mb geopotential is more coherent than that within the tropics during westerly QBO phases (Figure 3.5). This is not the case during easterly QBO phases, during which the tropical 300-mb geopotential signal is coherent throughout the entire tropics aside from over the eastern Pacific (Figure 3.6). The gap in coherence over the eastern Pacific is not present during boreal summertime, when the coherence of 300-mb geopotential anomalies associated with the MJO are at a maximum within the tropics. We hypothesized that this increased coherence over the eastern Pacific during boreal summertime is caused by the increased convective vigor within this region during boreal summertime that is associated with the MJO (Maloney and Esbensen 2003). Furthermore, since the fraction of variability associated with the MJO strongly depends on QBO phase during boreal wintertime but not during boreal summertime, perhaps the MJO itself is more sensitive to the QBO during boreal wintertime than boreal summertime. This may be related to the off-equatorial propagation of the convective signal of the MJO during boreal summertime, which displaces the MJO convective signal from the core of the tropical stratospheric QBO anomalies.

The global prevalence of 300-mb geopotential anomalies linked to the MJO is summarized within Figure 3.10. The fraction of intraseasonal variance in 300-mb geopotential that is associated with the MJO is maximized during boreal summertime and wintertime of easterly QBO phases,

during which approximately 12% to 13% of such variance can be explained by the MJO. The global signature of the MJO is least globally prominent during the boreal winter and spring of westerly QBO phases, when approximately 6% to 7% percent of intraseasonal anomalies in 300-mb geopotential are associated with the MJO. It is rather apparent that the QBO-blind analysis underestimates the global coherence of MJO teleconnections, with variance estimates that are less than those of either the westerly or easterly QBO phases. This is likely caused by the destructive interference of teleconnections during easterly and westerly QBO phases (Figure 3.7), since the locations of the teleconnections depends on QBO phase. Coh^2 considers the coherence of both the amplitude and phasing relationships between two time series across multiple samples, and since the amplitude and phasing of 300-mb teleconnections relative to the MJO depends on QBO phase, Coh^2 is reduced when all years are considered equivalently. It is therefore important for MJO-related analyses to consider the state of the QBO.

We have found that the global character of the MJO depends on QBO phase, which extends upon the body of research that suggests the tropical structure of the MJO is also dependent on the QBO. Our study summarizes the statistics of the relationship between the QBO and the extratropical teleconnections of the MJO, and makes suggestions for possible physical relationships based on mechanisms identified in prior studies. It would therefore be interesting to extend upon this study by using simple models, such as a linear baroclinic model, to identify the physical relationships between the QBO, the MJO, and extratropical teleconnections.

Table 3.1: Sample sizes and bounds of statistical significance for magnitude-squared coherence (Coh^2)

Analysis Separated by QBO State					
QBO State		DJF	MAM	JJA	SON
All	Samples	36	37	37	37
	$\alpha = 0.05$	0.0556	0.0530	0.0533	0.0535
Westerly	Samples	13	10	17	18
	$\alpha = 0.05$	0.151	0.187	0.114	0.108
Easterly	Samples	11	10	15	11
	$\alpha = 0.05$	0.175	0.183	0.128	0.169
Difference between Westerly and Easterly QBO					
QBO State		DJF	MAM	JJA	SON
	Samples		10,000		
Westerly	PC1: $\alpha = .05$	-0.0752	-0.140	-0.0782	-0.0444
minus	PC1: $\alpha = .95$	0.128	0.137	0.0917	0.0945
Easterly	PC2: $\alpha = .05$	-0.0854	-0.135	-0.0787	-0.0433
	PC2: $\alpha = .95$	0.127	0.138	0.0900	0.0963

[a] All confidence bounds were calculated using a Monte Carlo approach discussed in Section 3.2.3.

Table 3.2: Fraction of 2 to 96 day variability in 300-mb geopotential associated with the MJO

Season	QBO phase	Region/Hemisphere			
		Global	20°S to 20°N	30°N to 90°N	30°S to 90°S
DJF	All QBO	0.055	0.730	0.047	0.037
	Westerly QBO	0.068	0.074	0.069	0.059
	Easterly QBO	0.129	0.170	0.114	0.089
MAM	All QBO	0.042	0.56	0.033	0.032
	Westerly QBO	0.091	0.105	0.086	0.077
	Easterly QBO	0.091	0.107	0.084	0.075
JJA	All QBO	0.086	0.141	0.055	0.056
	Westerly QBO	0.106	0.150	0.083	0.081
	Easterly QBO	0.122	0.191	0.082	0.085
SON	All QBO	0.041	0.590	0.029	0.030
	Westerly QBO	0.063	0.087	0.049	0.047
	Easterly QBO	0.084	0.099	0.074	0.075

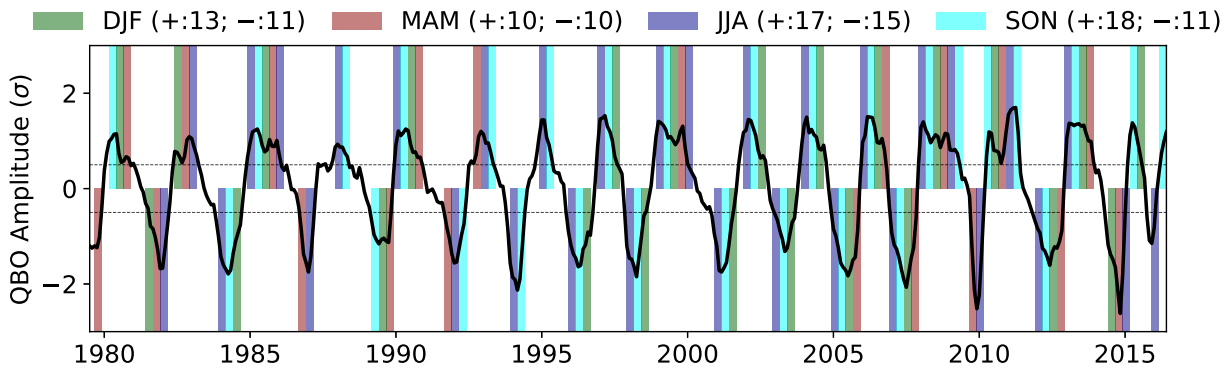

Figure 3.1: Standardized 50-mb zonal wind anomalies for January 1, 1980 through December 31, 2016. Seasons wherein the average QBO magnitude was greater than 0.5-σ are highlighted. The total number of seasons satisfying this criterion for QBO+ and QBO- phases are tallied within the legend above the figure.

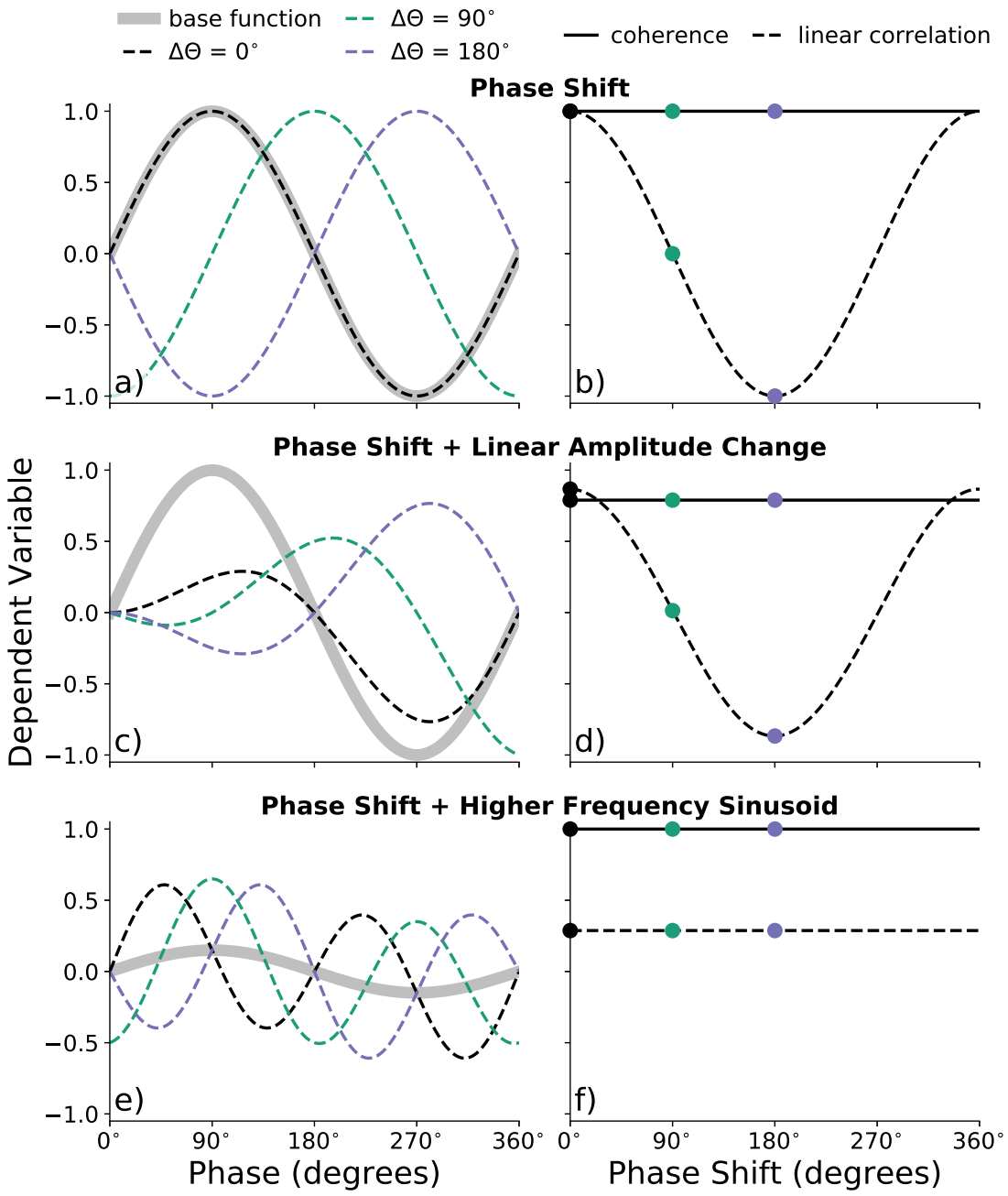

Figure 3.2: Example calculations of linear correlation and Coh^2 for various combinations of periodic signals. The linear correlation and Coh^2 are calculated between the base sinusoidal function (broad gray line) and the modified signals after applying an additional function to the base function. The presented cases are (a, b) a phase shift, (c, d) a phase shift plus a linear amplitude change, and (e, f) a phase shift plus a higher frequency sinusoid. Within subpanels (a), (c), and (e), examples of the modified signals are denoted by dashed lines, and the examples with phase shifts of 0°, 90°, and 180° are presented in black, teal, and purple, respectively. Subpanels (b), (d), and (f) show the Coh^2 and linear correlation between the base function and the phase shifted functions as a function of the phase shift. The phase shifts corresponding to the dashed lines in (a), (c), and (e) are demarcated by the colored dots in the corresponding linear correlation and Coh^2 plots (b), (d), and (f).

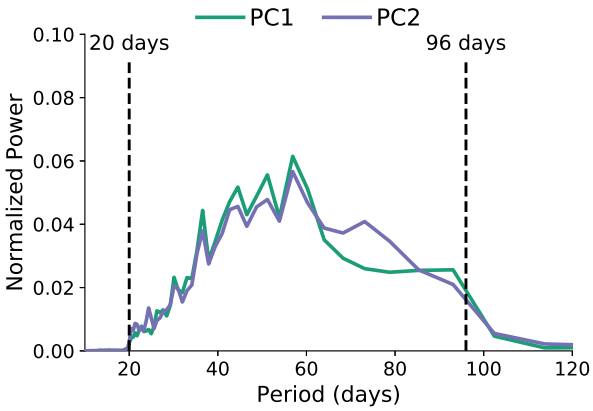

Figure 3.3: Normalized power spectra of the OMI principal components for the years 1980 through 2016, including all seasons and QBO phases. The 20 and 96 day periods are denoted by the vertical dashed lines, and are the bounds of the power spectrum considered within this study.

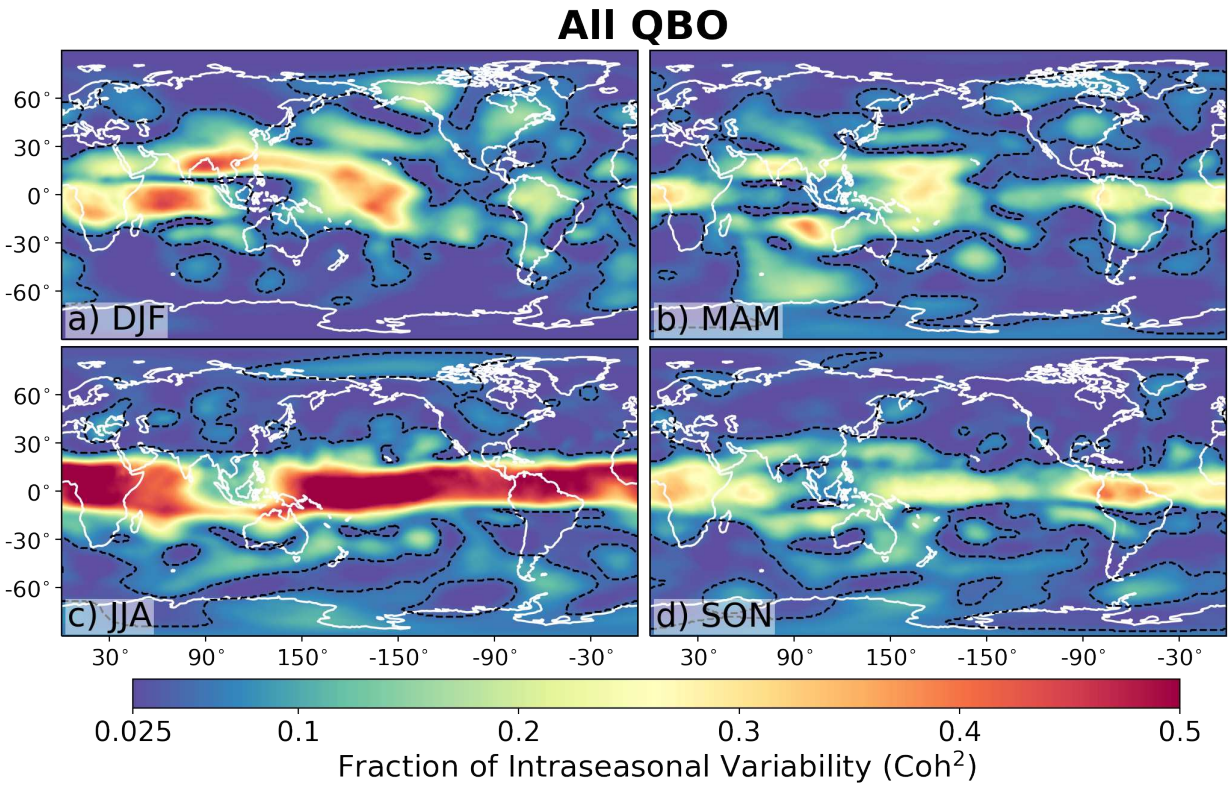

Figure 3.4: Magnitude-squared coherence (Coh^2) between the Outgoing Longwave Radiation MJO Index (OMI) and 300-mb geopotential anomalies from ERA-Interim for the years 1980-2016 for the four meteorological seasons. This Coh^2 value is also the fraction of variability in 300-mb geopotential that is associated with the MJO within the 30 to 96 day band. Regions where the Coh^2 surpasses the 95th-percentile confidence bounds estimated using a Monte Carlo approach are within the dashed contours. Confidence bounds are tabulated in Table 3.1.

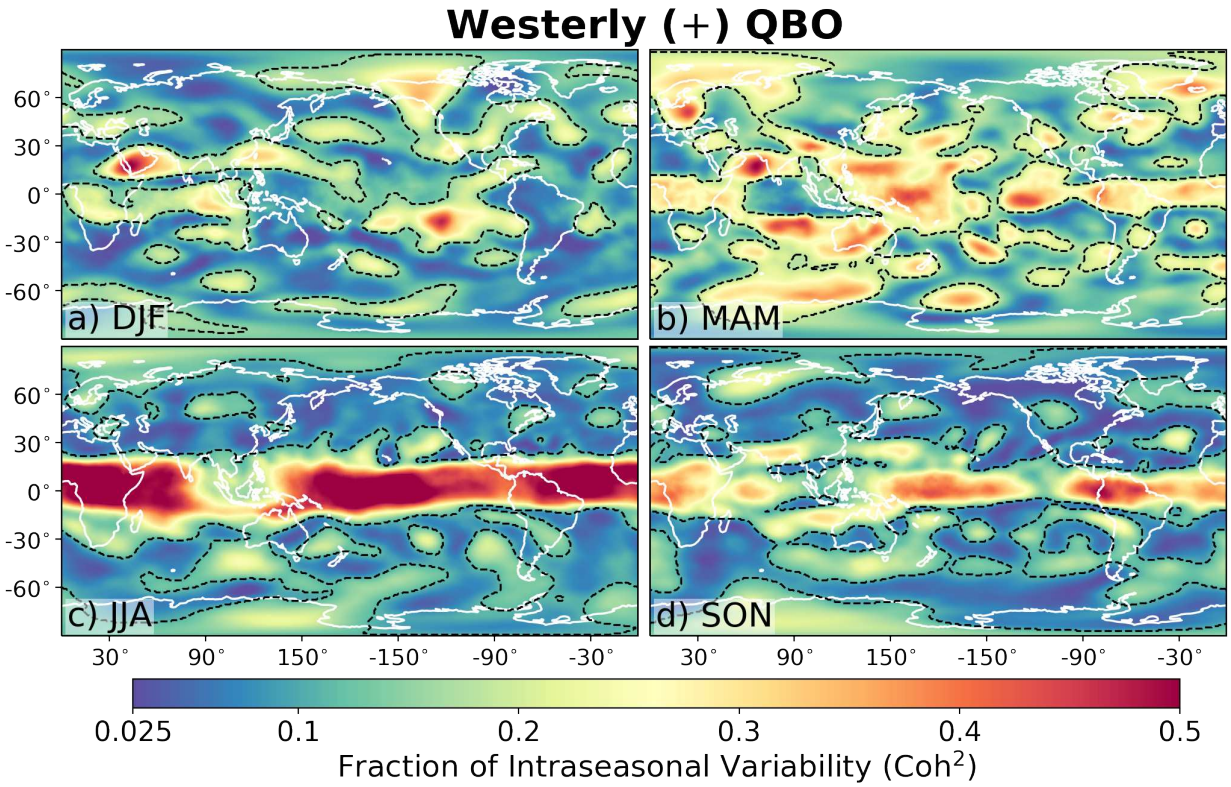

Figure 3.5: As in Figure 3.4, but for only westerly QBO states.

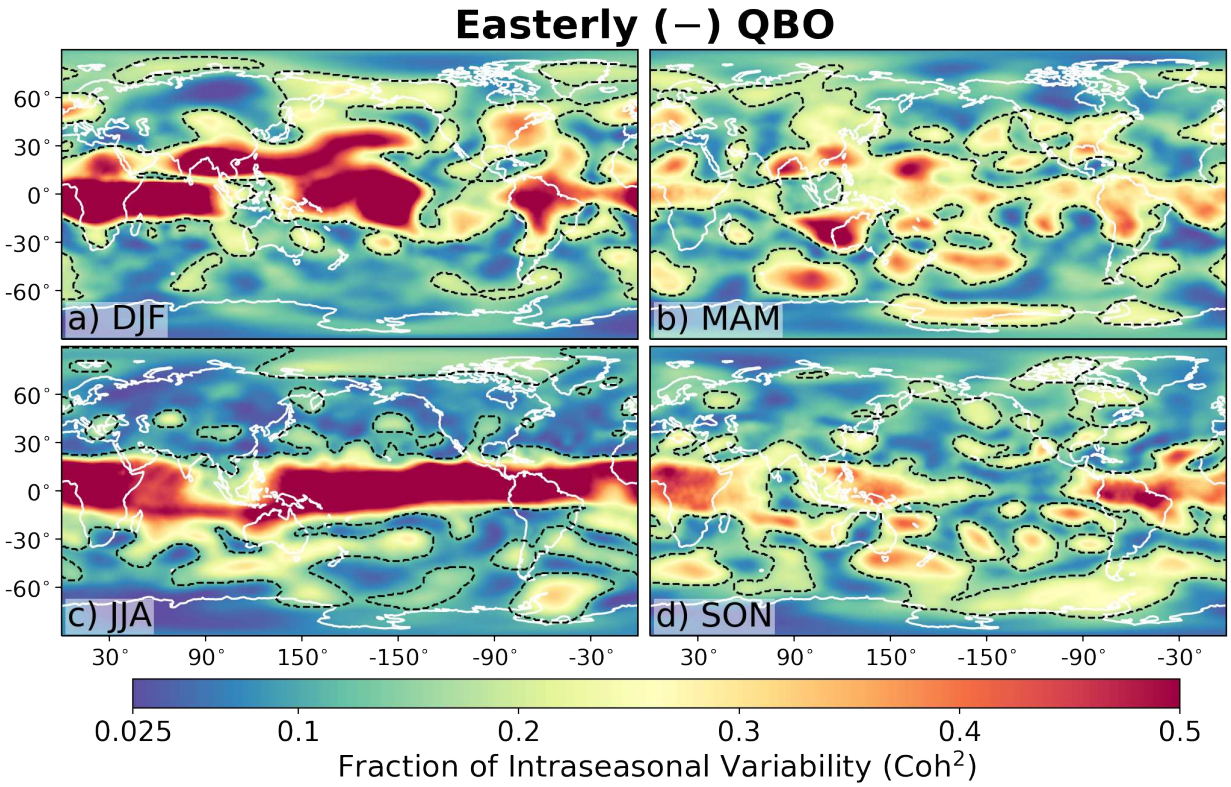

Figure 3.6: As in Figure 3.4, but for only easterly QBO states.

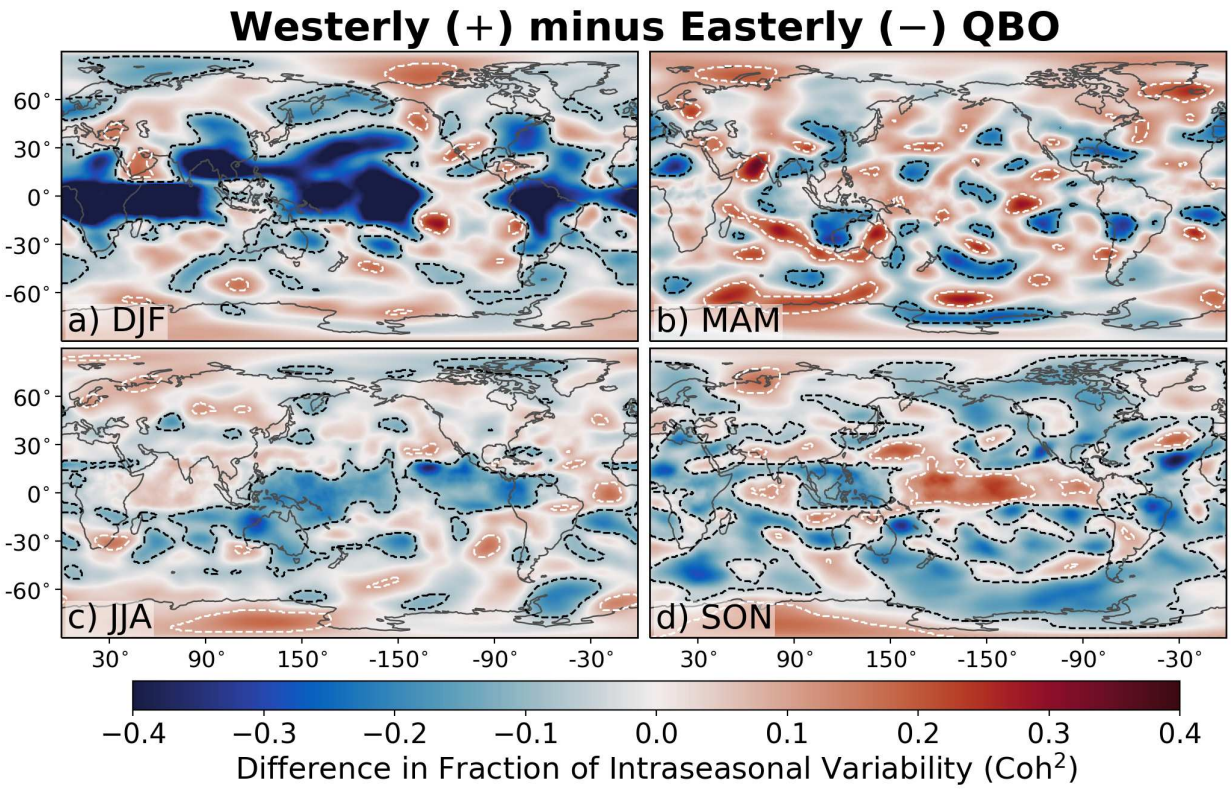

Figure 3.7: Difference between the Coh^2 between OMI PC1 (top) and PC2 (bottom) and 300-mb geopotential anomalies for easterly and westerly QBO phases. This Coh^2 value is also the fraction of variability in 300-mb geopotential that is associated with the MJO. Positive (negative) values denote a greater Coh^2 during westerly (easterly) QBO phases. Positive (negative) differences that are statistically differentiable from noise at the 90th percentile are within the white (black) dashed contours. Refer to Section 3.2.3 for a discussion of how the significance values, which are listed in Table 3.1, are calculated.

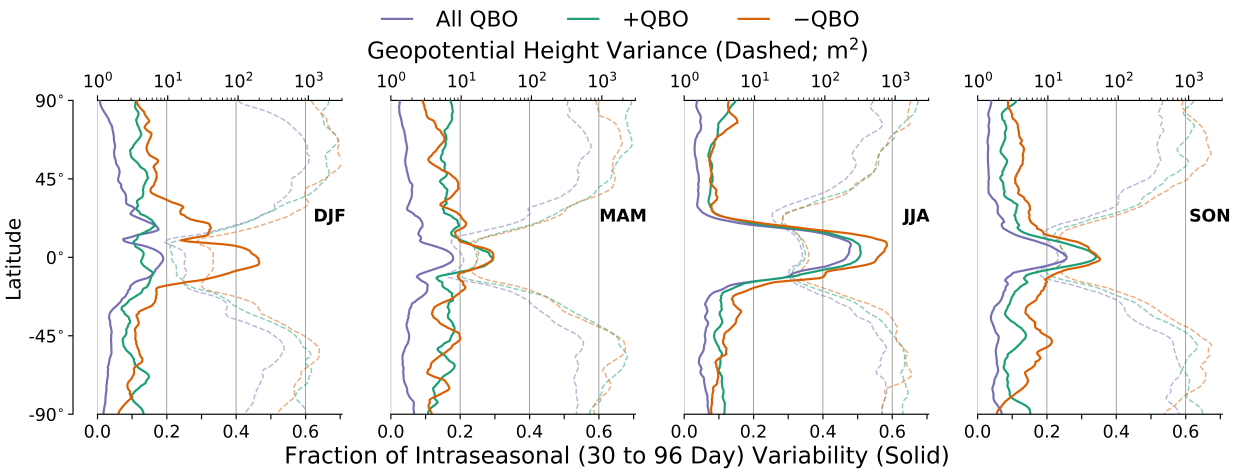

Figure 3.8: Longitudinal averages of (bottom; solid) the fraction of transient intraseasonal variability in 300-mb geopotential anomalies that can be linked to the MJO based on both PC1 and PC2 of OMI and (top; dashed) variance in 300-mb geopotential anomalies. The purple line corresponds to all QBO states and includes all years from 1980 through 2017, while the green and orange lines correspond to the westerly and easterly QBO phases respectively and only include years as detailed in Figure 3.1.

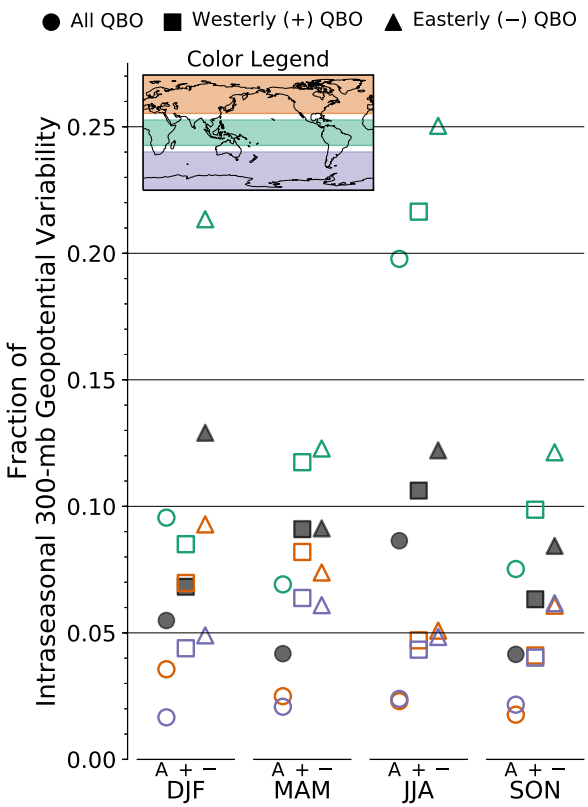

Figure 3.9: Fraction of transient intraseasonal (2 to 96 day) 300-mb geopotential variance linked to the MJO during the DJF/MAM/JJA/SON seasons and across various sub-domains of the globe. The following sub-domains are represented: solid fill, global average; hollow green, 20°S to 20°N; hollow orange, 30°N to 90°N; hollow purple, 30°S to 90°S. The dependence on QBO phase is also shown for each season, with circles representing the QBO-blind mean, squares the westerly (−) QBO states, and triangles the easterly (+) QBO states. The values are tabulated within Table 3.2.

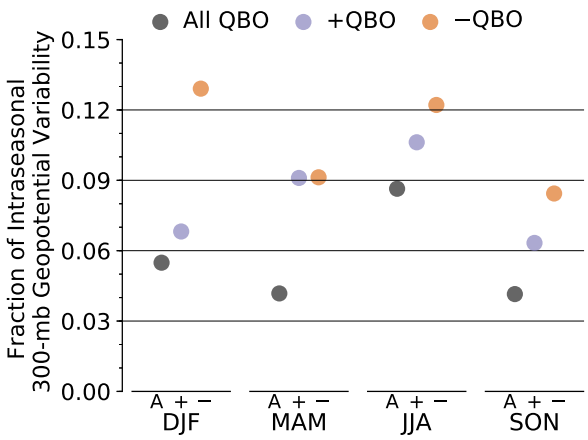

Figure 3.10: Global averages of the fraction of transient intraseasonal (2 to 96) day 300-mb geopotential variance linked to the MJO for each season and QBO state. The values are tabulated within Table 3.2.

Chapter 4

Overall Summary and Conclusions

As highlighted by this thesis, the Madden-Julian Oscillation (MJO) is connected to other atmospheric processes across a wide range of scales, from the mesoscales of individual tropical convective systems to the global circulation patterns of extratropical teleconnections. The complexity of the interactions between the MJO and the global atmospheric system complicate the inference of scientifically meaningful results regarding their existence and prevalence. Through two targeted approaches, this thesis has expanded upon the body of literature that suggests that the MJO influences and is influenced by atmospheric processes across a broad range of scales, with different origins and structure from that of the MJO. The cross-scale and global prevalence of the MJO was analyzed throughout two separate studies, one of which used a cloud-resolving model to investigate the mesoscale structure of the MJO and the other of which used cross-spectral analysis to quantify the prevalence of the MJO within the overall climate system. The main findings of these two studies are as follows:

1. The morphology of convective cells within the convectively enhanced lobe of the boreal summertime MJO exhibits a pronounced progressive relationship, which suggests that a cross-scale relationship exists between messocale convective structures and the regional convective anomaly of the MJO.

2. The global structure of the MJO depends on both the season and phase of the QBO, which extends upon the body of research that has shown the MJO and its teleconnections to be strongly dependent on the background state of the atmosphere.

The first study investigated the cross-scale relationship between mesoscale convective cloud morphology and the regional anomalies of the MJO using a cloud-resolving model (CRM). The entirety of a canonical boreal summertime MJO event was simulated using the CRM, and the convective cloud features were tracked and logged according to their location within the convective

dipole of the MJO. The simulation successfully identified the spatial and temporal bounds of the intraseasonal rainfall anomalies based on a comparison with Global Precipitation Measurement Mission (GPM) satellite observations, which suggests that the location and intensity of convective elements within the simulation were similar to those in nature. The interactions between the mesoscale convective cells and regional convective anomaly of the MJO were then analyzed using two separate techniques; spectral analysis and phase compositing. Both techniques generated similar statistics, with the spectral analysis offering detailed insights into the progressive relationship between convective cloud morphology and the MJO. Namely, the intraseasonal relationship between cloud morphology and the convectively enhanced regions of the MJO is as follows: increased cell longevity in the initial phases, followed by increased cell number in the intermediate phases, progressing into increased cell expanse in the terminal phases. This relationship comprises 22.8% of all variability in convective cell number, 7.8% of all variability in convective cell expanse, and 17.3% of all variability in convective cell longevity throughout the simulation. The variability in these three morphology characteristics appears to be related to bulk thermodynamic and kinematic atmospheric characteristics, such as convective instability and vertical wind shear. While the bulk thermodynamic and kinematic characteristics of the atmosphere seem to most influence convective cell expanse and longevity, the number of convective cells appears to be tied to another source of variability not identified within this study.

The second study approached the global structure of the MJO from a statistical perspective and quantified the prevalence of the MJO within the overall climate system using cross-spectral analysis. Cross-spectral analysis measures the relationship between two periodic time series, separated into each harmonic mode, and provides an estimate of the amount of variability in one time series that can be explained by variability in another time series. Magnitude-squared coherence (Coh^2), a derivative of cross-spectral analysis, extends upon this concept and quantifies the fraction of variability in one periodic time series that can be explained by variability in another periodic time series, separated into each harmonic mode. We thereby used Coh^2 to estimate the fraction of upper-tropospheric geopotential variability that can be linked to the MJO at each location across

the globe. The analysis was separated into each meteorological season and phase of the QBO to test the dependence of the global signature of the MJO on the background state of the atmosphere. It was found that the global upper-tropospheric signature of the MJO strongly depends on both the season and phase of the QBO, with easterly QBO phases during either boreal summertime or boreal wintertime leading to the most coherent global anomalies. This finding is consistent with previous work that has shown the tropical convective structure of the MJO to be longer lasting and more persistent during easterly QBO phases (Hendon and Abhik 2018; Lee and Klingaman 2018; Son et al. 2017). Additionally, the tropical upper-tropospheric geopotential structure of the MJO was found to be most coherent during boreal summertime, especially over the eastern Pacific. This may be related to the greater amount of MJO-driven convection within the eastern Pacific during boreal summertime (Maloney and Esbensen 2003), which could permit the influences of the MJO to spread eastward from the Indo-Pacific warm pool more coherently during boreal summertime, or the presence of a westerly wave duct within the Eastern Pacific during boreal wintertime (Webster and Holton 1982) that could disrupt the signal of the MJO within this region.

Within a broader context, this thesis highlights the prevalence of connections between the MJO and processes of different physical origin and scale to that of the MJO. Correctly simulating the MJO within global models is therefore critical to the accurate simulation of processes across the entire globe. However, as highlighted by the cloud-resolving simulation, the Madden-Julian Oscillation is related to the morphology of mesoscale convective structures within the tropics and is thereby associated with both planetary-scale and mesoscale convective anomalies. It is therefore important to accurately simulate the mesoscale convective structure of the tropics in order to capture the full character of the MJO, whether through direct representation of clouds or through robust parameterizations. This finding has also been supported by other research that has shown more realistic cloud parameterizations to improve the simulation of the MJO and its global teleconnections within global simulations (Khairoutdinov and Randall 2001; Thayer-Calder and Randall 2009; Zhou et al. 2012). The results of the cloud-resolving simulation may be used to improve the sub-grid scale cloud parameterizations within such simulations. The cross-scale relationship

identified within this thesis may be used to constrain the sub-grid scale cloud properties within the global simulation according to the state of the MJO, thereby indirectly constraining the global circulation model to the relationships resolved within cloud-resolving simulation.

4.1 Future Work

Numerous additional pathways of research could extend from the work presented within this thesis. Cross-scale relationships between the MJO and other atmospheric processes remains an open topic of research, and this thesis offers numerous tangential avenues for related future research. For example, to what extent does the cross-scale relationship identified within the cloud-resolving simulation modulate the longevity and spatial expanse of MJO events? A relationship has been discovered, but is it important for the overall evolution of the MJO? Additionally, numerous synoptic-scale disturbances move westward into the Maritime Continent throughout the simulation and cause deviations from the otherwise predominantly intraseasonal anomalies in the 850-mb wind field. It was not tested whether these westward moving waves are the prototypical easterly waves commonly observed within this region, but, if so, do easterly waves have an impact on the eastward propagation of the MJO over the Maritime Continent? Within the simulated case, two of the westward moving waves develop into weak tropical circulations, which were similarly documented in observations as strong tropical storms. Do these tropical circulations modulate the boreal summertime MJO, or does the relationship only extend downscale, wherein the MJO has been shown to modulate the frequency and intensity of such tropical easterly waves? From a global perspective, physical mechanisms driving the dependence of the coherence in extratropical upper-tropospheric geopotential anomalies on QBO phase have been proposed but not yet fully explored. The exploration of such a causal mechanism may provide insights into how the MJO interacts with atmospheric processes on a longer timescale than itself. Furthermore, the elucidation of physical mechanisms could improve subseasonal predictability, wherein the disparities between the extratropical patterns during QBO phases could be used to forecast the likelihood of certain circulation patterns within a given season and QBO phase. The analysis presented within this thesis could

plausibly be used for a similar type of stochastic forecast, although more confidence could be placed in the extended forecasts if the physical mechanisms driving their existence are understood.

Chapter 4Bibliography

Adames, A. F., and D. Kim, 2016a: The MJO as a dispersive, convectively coupled moisture wave: Theory and observations. *Journal of the Atmospheric Sciences*, **73 (3)**, 913–941, doi: 10.1175/JAS-D-15-0170.1.

Adames, Á. F., and D. Kim, 2016b: The MJO as a dispersive, convectively coupled moisture wave: Theory and observations. *Journal of the Atmospheric Sciences*, **73 (3)**, 913–941.

Adames, Ã. F., and J. M. Wallace, 2015: Three–dimensional structure and evolution of the moisture field in the MJO. *Journal of the Atmospheric Sciences*, **72 (10)**, 3733–3754, doi: 10.1175/JAS-D-15-0003.1.

Alvarez, M. S., C. S. Vera, and G. N. Kiladis, 2017: MJO modulating the activity of the leading mode of intraseasonal variability in South America. *Atmosphere*, **8 (12)**.

Alvarez, M. S., C. S. Vera, G. N. Kiladis, and B. Liebmann, 2016: Influence of the Madden Julian Oscillation on precipitation and surface air temperature in South America. *Climate dynamics*, **46 (1-2)**, 245–262.

Arbic, B. K., R. B. Scott, G. R. Flierl, A. J. Morten, J. G. Richman, and J. F. Shriver, 2012: Nonlinear cascades of surface oceanic geostrophic kinetic energy in the frequency domain. *Journal of Physical Oceanography*, **42 (9)**, 1577–1600, doi:10.1175/JPO-D-11-0151.1.

Ashok, K., S. K. Behera, S. A. Rao, H. Weng, and T. Yamagata, 2007: El Niño Modoki and its possible teleconnection. *Journal of Geophysical Research: Oceans*, **112 (C11)**.

Baggett, C. F., E. A. Barnes, E. D. Maloney, and B. D. Mundhenk, 2017: Advancing atmospheric river forecasts into subseasonal-to-seasonal time scales. *Geophysical Research Letters*, **44 (14)**, 7528–7536, doi:10.1002/2017GL074434.

Baggett, C. F., K. M. Nardi, S. J. Childs, S. N. Zito, E. A. Barnes, and E. D. Maloney, 2018: Skillful subseasonal forecasts of weekly tornado and hail activity using the Madden-Julian oscillation. *Journal of Geophysical Research: Atmospheres*, **0 (0)**, doi:10.1029/2018JD029059.

Baldwin, M. P., and T. J. Dunkerton, 1998: Quasi-biennial modulation of the southern hemisphere stratospheric polar vortex. *Geophysical Research Letters*, **25 (17)**, 3343–3346, doi: 10.1029/98GL02445.

Baldwin, M. P., and Coauthors, 2001: The quasi-biennial oscillation. *Reviews of Geophysics*, **39 (2)**, 179–229, doi:10.1029/1999RG000073.

Barnes, H. C., and R. A. Houze Jr, 2013a: The precipitating cloud population of the Madden–Julian Oscillation over the Indian and west Pacific Oceans. *Journal of Geophysical Research: Atmospheres*, **118 (13)**, 6996–7023.

Barnes, H. C., and R. A. Houze Jr, 2013b: The precipitating cloud population of the Madden–Julian Oscillation over the Indian and west Pacific Oceans. *Journal of Geophysical Research: Atmospheres*, **118 (13)**, 6996–7023.

Barnes, H. C., and R. A. Houze Jr, 2013c: The precipitating cloud population of the Madden–Julian Oscillation over the Indian and west Pacific Oceans. *Journal of Geophysical Research: Atmospheres*, **118 (13)**, 6996–7023.

Bessafi, M., and M. C. Wheeler, 2006: Modulation of south Indian Ocean tropical cyclones by the Madden–Julian oscillation and convectively coupled equatorial waves. *Monthly Weather Review*, **134 (2)**, 638–656.

Biasutti, M., S. E. Yuter, C. D. Burleyson, and A. H. Sobel, 2012: Very high resolution rainfall patterns measured by TRMM precipitation radar: seasonal and diurnal cycles. *Climate dynamics*, **39 (1-2)**, 239–258.

Boer, G. J., and K. Hamilton, 2008: QBO influence on extratropical predictive skill. *Climate Dynamics*, **31 (7)**, 987–1000, doi:10.1007/s00382-008-0379-5, URL https://doi.org/10.1007/s00382-008-0379-5.

Cassou, C., 2008: Intraseasonal interaction between the Madden–Julian oscillation and the North Atlantic Oscillation. *Nature*, **455 (7212)**, 523.

Chang, C., and C. Miller III, 1977: Comparison of easterly waves in the tropical Pacific during two contrasting periods of sea surface temperature anomalies. *Journal of the Atmospheric Sciences*, **34 (4)**, 615–628.

Chang, E. K., 1995: The influence of Hadley circulation intensity changes on extratropical climate in an idealized model. *Journal of the atmospheric sciences*, **52 (11)**, 2006–2024.

Cotton, W. R., and Coauthors, 2003: RAMS 2001: Current status and future directions. *Meteorology and Atmospheric Physics*, **82 (1)**, 5–29, doi:10.1007/s00703-001-0584-9.

Dee, D. P., and Coauthors, 2011: The ERA-Interim reanalysis: configuration and performance of the data assimilation system. *Quarterly Journal of the Royal Meteorological Society*, **137 (656)**, 553–597, doi:10.1002/qj.828.

DeMott, P. J., and Coauthors, 2010: Predicting global atmospheric ice nuclei distributions and their impacts on climate. *Proceedings of the National Academy of Sciences*.

Diaz, H. F., M. P. Hoerling, and J. K. Eischeid, 2001: ENSO variability, teleconnections and climate change. *International Journal of Climatology*, **21 (15)**, 1845–1862.

Dunkerton, T. J., 1991: Intensity variation and coherence of 3-6 day equatorial waves. *Geophysical Research Letters*, **18 (8)**, 1469–1472, doi:10.1029/91GL01780.

Fierro, A. O., J. Simpson, M. A. LeMone, J. M. Straka, and B. F. Smull, 2009: On how hot towers fuel the Hadley cell: An observational and modeling study of line-organized convection in the equatorial trough from TOGA COARE. *Journal of the Atmospheric Sciences*, **66 (9)**, 2730–2746.

Folland, C. K., A. A. Scaife, J. Lindesay, and D. B. Stephenson, 2012: How potentially predictable is northern European winter climate a season ahead? *International Journal of Climatology*, **32 (6)**, 801–818, doi:10.1002/joc.2314.

Guan, B., and D. E. Waliser, 2015: Detection of atmospheric rivers: Evaluation and application of an algorithm for global studies. *Journal of Geophysical Research: Atmospheres*, **120 (24)**, 12 514–12 535, doi:10.1002/2015JD024257.

Guevara, M. A., and M. Corsi-Cabrera, 1996: EEG coherence or EEG correlation? *International Journal of Psychophysiology*, **23 (3)**, 145–153, doi:10.1016/S0167-8760(96)00038-4.

Haertel, P., K. Straub, and A. Budsock, 2015: Transforming circumnavigating kelvin waves that initiate and dissipate the Madden-Julian oscillation. *Quarterly Journal of the Royal Meteorological Society*, **141 (690)**, 1586–1602, doi:10.1002/qj.2461.

Hall, J. D., A. J. Matthews, and D. J. Karoly, 2001: The modulation of tropical cyclone activity in the Australian region by the Madden–Julian oscillation. *Monthly Weather Review*, **129 (12)**, 2970–2982.

Harrington, J. Y., 1997: The effects of radiative and microphysical processes on simulated warm and transition season arctic stratus. Ph.D. thesis, COLORADO STATE UNIVERSITY.

Hayashi, Y., 1980: Estimation of nonlinear energy transfer spectra by the cross–spectral method. *Journal of the Atmospheric Sciences*, **37 (2)**, 299–307, doi:10.1175/1520-0469(1980)037<0299:EONETS>2.0.CO;2.

Henderson, S. A., E. D. Maloney, and E. A. Barnes, 2016a: The influence of the Madden–Julian oscillation on northern hemisphere winter blocking. *Journal of Climate*, **29 (12)**, 4597–4616, doi:10.1175/JCLI-D-15-0502.1.

Henderson, S. A., E. D. Maloney, and E. A. Barnes, 2016b: The influence of the Madden-Julian Oscillation on northern hemisphere winter blocking. *Journal of Climate*, **29 (12)**, 4597–4616, doi:10.1175/JCLI-D-15-0502.1.

Henderson, S. A., E. D. Maloney, and S.-W. Son, 2017: Madden-Julian oscillation pacific teleconnections: The impact of the basic state and MJO representation in general circulation models. *Journal of Climate*, **30 (12)**, 4567–4587, doi:10.1175/JCLI-D-16-0789.1.

Hendon, H. H., and S. Abhik, 2018: Differences in vertical structure of the Madden-Julian oscillation associated with the quasi-biennial oscillation. *Geophysical Research Letters*, **45 (9)**, 4419–4428, doi:10.1029/2018GL077207.

Hendon, H. H., and B. Liebmann, 1991: The structure and annual variation of antisymmetric fluctuations of tropical convection and their association with Rossby–gravity waves. *Journal of the atmospheric sciences*, **48 (19)**, 2127–2140.

Hendon, H. H., and B. Liebmann, 1994a: Organization of convection within the Madden–Julian oscillation. *Journal of Geophysical Research: Atmospheres*, **99 (D4)**, 8073–8083.

Hendon, H. H., and B. Liebmann, 1994b: Organization of convection within the Madden–Julian oscillation. *Journal of Geophysical Research: Atmospheres*, **99 (D4)**, 8073–8083.

Hendon, H. H., and B. Liebmann, 1994c: Organization of convection within the Madden-Julian oscillation. *Journal of Geophysical Research: Atmospheres*, **99 (D4)**, 8073–8083, doi:10.1029/94JD00045.

Hendon, H. H., and M. L. Salby, 1994: The life cycle of the Madden–Julian oscillation. *Journal of the Atmospheric Sciences*, **51 (15)**, 2225–2237.

Holton, J. R., and H.-C. Tan, 1980: The influence of the equatorial quasi-biennial oscillation on the global circulation at 50 mb. *Journal of the Atmospheric Sciences*, **37 (10)**, 2200–2208.

Hoskins, B. J., and D. J. Karoly, 1981: The steady linear response of a spherical atmosphere to thermal and orographic forcing. *Journal of the Atmospheric Sciences*, **38 (6)**, 1179–1196, doi:10.1175/1520-0469(1981)038<1179:TSLROA>2.0.CO;2.

Hou, A. Y., and Coauthors, 2014: The global precipitation measurement mission. *Bulletin of the American Meteorological Society*, **95 (5)**, 701–722.

Jiang, X., Ã. F. Adames, M. Zhao, D. Waliser, and E. Maloney, 2018: A unified moisture mode framework for seasonality of the Madden–Julian oscillation. *Journal of Climate*, **31 (11)**, 4215–4224, doi:10.1175/JCLI-D-17-0671.1.

Jiang, X., and Coauthors, 2015: Vertical structure and physical processes of the Madden–Julian oscillation: Exploring key model physics in climate simulations. *Journal of Geophysical Research: Atmospheres*, **120 (10)**, 4718–4748.

Johnson, R. H., and D. C. Kriete, 1982: Thermodynamic and circulation characteristics, of winter monsoon tropical mesoscale convection. *Monthly Weather Review*, **110 (12)**, 1898–1911, doi:10.1175/1520-0493(1982)110<1898:TACCOW>2.0.CO;2.

Kawatani, Y., S. Watanabe, K. Sato, T. J. Dunkerton, S. Miyahara, and M. Takahashi, 2010: The roles of equatorial trapped waves and internal inertiaâĂŞgravity waves in driving the quasi-biennial oscillation. Part I: Zonal mean wave forcing. *Journal of the Atmospheric Sciences*, **67 (4)**, 963–980, doi:10.1175/2009JAS3222.1.

Kemball-Cook, S. R., and B. C. Weare, 2001: The onset of convection in the Madden-Julian oscillation. *Journal of Climate*, **14 (5)**, 780–793, doi:10.1175/1520-0442(2001)014<0780:TOOCIT>2.0.CO;2.

Khairoutdinov, M. F., and D. A. Randall, 2001: A cloud resolving model as a cloud parameterization in the NCAR Community Climate System Model: Preliminary results. *Geophysical Research Letters*, **28 (18)**, 3617–3620.

Kikuchi, K., B. Wang, and Y. Kajikawa, 2012a: Bimodal representation of the tropical intraseasonal oscillation. *Climate dynamics*, **38 (9-10)**, 1989–2000.

Kikuchi, K., B. Wang, and Y. Kajikawa, 2012b: Bimodal representation of the tropical intraseasonal oscillation. *Climate Dynamics*, **38 (9)**, 1989–2000, doi:10.1007/s00382-011-1159-1.

Kiladis, G. N., J. Dias, K. H. Straub, M. C. Wheeler, S. N. Tulich, K. Kikuchi, K. M. Weickmann, and M. J. Ventrice, 2014: A comparison of OLR and circulation-based indices for tracking the MJO. *Monthly Weather Review*, **142 (5)**, 1697–1715.

Kiladis, G. N., K. H. Straub, and P. T. Haertel, 2005: Zonal and vertical structure of the Madden-Julian Oscillation. *Journal of the Atmospheric Sciences*, **62 (8)**, 2790–2809, doi: 10.1175/JAS3520.1.

Kiladis, G. N., and K. M. Weickmann, 1992: Circulation anomalies associated with tropical convection during northern winter. *Monthly weather review*, **120 (9)**, 1900–1923.

Klemp, J. B., and R. B. Wilhelmson, 1978: The simulation of three-dimensional convective storm dynamics. *Journal of the Atmospheric Sciences*, **35 (6)**, 1070–1096.

Klotzbach, P. J., 2010: On the Madden–Julian oscillation–Atlantic hurricane relationship. *Journal of Climate*, **23 (2)**, 282–293.

Lane, T. P., M. J. Reeder, and T. L. Clark, 2001: Numerical modeling of gravity wave generation by deep tropical convection. *Journal of the atmospheric sciences*, **58 (10)**, 1249–1274.

Lee, J. C. K., and N. P. Klingaman, 2018: The effect of the quasi-biennial oscillation on the MaddenâĂŞJulian oscillation in the Met Office Unified Model Global Ocean Mixed Layer configuration. *Atmospheric Science Letters*, **19 (5)**, e816, doi:10.1002/asl.816.

LeMone, M. A., E. J. Zipser, and S. B. Trier, 1998: The role of environmental shear and thermodynamic conditions in determining the structure and evolution of mesoscale convective systems during TOGA COARE. *Journal of the Atmospheric Sciences*, **55 (23)**, 3493–3518, doi: 10.1175/1520-0469(1998)055<3493:TROESA>2.0.CO;2.

Li, R. C. Y., and W. Zhou, 2013: Modulation of western North Pacific tropical cyclone activity by the iso. Part I: Genesis and intensity. *Journal of Climate*, **26 (9)**, 2904–2918, doi:10.1175/JCLI-D-12-00210.1.

Liebmann, B., and H. H. Hendon, 1990: Synoptic-scale disturbances near the equator. *Journal of the Atmospheric Sciences*, **47 (12)**, 1463–1479, doi:10.1175/1520-0469(1990)047<1463:SSDNTE>2.0.CO;2.

Liebmann, B., H. H. Hendon, and J. D. Glick, 1994: The relationship between tropical cyclones of the western Pacific and Indian Oceans and the Madden–Julian oscillation. *Journal of the Meteorological Society of Japan. Ser. II*, **72 (3)**, 401–412.

Lindzen, R. S., and J. R. Holton, 1968: A theory of the quasi-biennial oscillation. *Journal of the Atmospheric Sciences*, **25 (6)**, 1095–1107, doi:10.1175/1520-0469(1968)025<1095:ATOTQB>2.0.CO;2.

Ling, J., and Coauthors, 2017: Challenges and Opportunities in MJO Studies. *Bulletin of the American Meteorological Society*, **98 (2)**, ES53–ES56, doi:10.1175/BAMS-D-16-0283.1.

Lorenz, E. N., 1969: The nature of the global circulation of the atmosphere: A present view. *The global circulation of the atmosphere*, 3–23.

Love, B. S., A. J. Matthews, and G. M. Lister, 2011: The diurnal cycle of precipitation over the Maritime Continent in a high-resolution atmospheric model. *Quarterly Journal of the Royal Meteorological Society*, **137 (657)**, 934–947.

Madden, R. A., 1986a: Seasonal variations of the 40-50 day oscillation in the tropics. *Journal of the atmospheric sciences*, **43 (24)**, 3138–3158.

Madden, R. A., 1986b: Seasonal variations of the 40-50 day oscillation in the tropics. *Journal of the atmospheric sciences*, **43 (24)**, 3138–3158.

Madden, R. A., and P. R. Julian, 1971: Detection of a 40–50 day oscillation in the zonal wind in the tropical Pacific. *Journal of the atmospheric sciences*, **28 (5)**, 702–708.

Madden, R. A., and P. R. Julian, 1972: Description of global-scale circulation cells in the tropics with a 40–50 day period. *Journal of the atmospheric sciences*, **29 (6)**, 1109–1123.

Madden, R. A., and P. R. Julian, 1994: Observations of the 40–50-day tropical oscillation-A review. *Monthly Weather Review*, **122 (5)**, 814–837.

Majda, A. J., and S. N. Stechmann, 2009: The skeleton of tropical intraseasonal oscillations. *Proceedings of the National Academy of Sciences*, **106 (21)**, 8417–8422, doi:10.1073/pnas.0903367106.

Maloney, E. D., and S. K. Esbensen, 2003: The amplification of east Pacific Madden–Julian oscillation convection and wind anomalies during June–November. *Journal of climate*, **16 (21)**, 3482–3497.

Maloney, E. D., and D. L. Hartmann, 2000: Modulation of eastern North Pacific hurricanes by the Madden–Julian oscillation. *Journal of climate*, **13 (9)**, 1451–1460.

Matthews, A. J., B. J. Hoskins, and M. Masutani, 2006: The global response to tropical heating in the Madden-Julian oscillation during the northern winter. *Quarterly Journal of the Royal Meteorological Society*, **130 (601)**, 1991–2011, doi:10.1256/qj.02.123.

Meyers, M. P., R. L. Walko, J. Y. Harrington, and W. R. Cotton, 1997: New RAMS cloud microphysics parameterization. Part II: The two-moment scheme. *Atmospheric Research*, **45 (1)**, 3–39.

Mundhenk, B. D., E. A. Barnes, and E. D. Maloney, 2016: All-season climatology and variability of atmospheric river frequencies over the North Pacific. *Journal of Climate*, **29 (13)**, 4885–4903, doi:10.1175/JCLI-D-15-0655.1.

Mundhenk, B. D., E. A. Barnes, E. D. Maloney, and C. F. Baggett, 2018: Skillful empirical subseasonal prediction of landfalling atmospheric river activity using the Madden–Julian oscillation and quasi-biennial oscillation. *npj Climate and Atmospheric Science*, **1 (1)**, 7.

Naujokat, B., 1986: An update of the observed quasi-biennial oscillation of the stratospheric winds over the tropics. *Journal of the Atmospheric Sciences*, **43 (17)**, 1873–1877.

Nesbitt, S. W., and E. J. Zipser, 2003: The diurnal cycle of rainfall and convective intensity according to three years of TRMM measurements. *Journal of Climate*, **16 (10)**, 1456–1475.

Pascoe, C. L., L. J. Gray, S. A. Crooks, M. N. Juckes, and M. P. Baldwin, 2005: The quasi-biennial oscillation: Analysis using ERA-40 data. *Journal of Geophysical Research: Atmospheres*, **110 (D8)**, doi:10.1029/2004JD004941.

Peatman, S. C., A. J. Matthews, and D. P. Stevens, 2014a: Propagation of the Madden–Julian Oscillation through the Maritime Continent and scale interaction with the diurnal cycle of precipitation. *Quarterly Journal of the Royal Meteorological Society*, **140 (680)**, 814–825.

Peatman, S. C., A. J. Matthews, and D. P. Stevens, 2014b: Propagation of the Madden–Julian Oscillation through the Maritime Continent and scale interaction with the diurnal cycle of precipitation. *Quarterly Journal of the Royal Meteorological Society*, **140 (680)**, 814–825.

Petersen, W. A., and S. A. Rutledge, 2001: Regional variability in tropical convection: Observations from TRMM. *Journal of Climate*, **14 (17)**, 3566–3586, doi:10.1175/1520-0442(2001)014<3566:RVITCO>2.0.CO;2.

Pohl, B., Y. Richard, and N. Fauchereau, 2007: Influence of the Madden–Julian oscillation on southern African summer rainfall. *Journal of Climate*, **20 (16)**, 4227–4242.

Powell, S. W., 2017: Successive MJO propagation in MERRA-2 reanalysis. *Geophysical Research Letters*, **44 (10)**, 5178–5186, doi:10.1002/2017GL073399.

Powell, S. W., and R. A. Houze, 2013: The cloud population and onset of the Madden-Julian oscillation over the Indian Ocean during DYNAMO-AMIE. *Journal of Geophysical Research: Atmospheres*, **118 (21)**, 11,979–11,995, doi:10.1002/2013JD020421.

Randel, W. J., and F. Wu, 2005: Kelvin wave variability near the equatorial tropopause observed in GPS radio occultation measurements. *Journal of Geophysical Research: Atmospheres*, **110 (D3)**, doi:10.1029/2004JD005006.

Rauniyar, S. P., and K. J. Walsh, 2011: Scale interaction of the diurnal cycle of rainfall over the Maritime Continent and Australia: Influence of the MJO. *Journal of Climate*, **24 (2)**, 325–348.

Reynolds, R. W., N. A. Rayner, T. M. Smith, D. C. Stokes, and W. Wang, 2002: An improved in situ and satellite SST analysis for climate. *Journal of climate*, **15 (13)**, 1609–1625.

Riddle, E. E., M. B. Stoner, N. C. Johnson, M. L. L'Heureux, D. C. Collins, and S. B. Feldstein, 2013: The impact of the MJO on clusters of wintertime circulation anomalies over the North American region. *Climate Dynamics*, **40 (7)**, 1749–1766, doi:10.1007/s00382-012-1493-y.

Riehl, H., and J. S. Malkus, 1957: On the heat balance and maintenance of circulation in the trades. *Quarterly Journal of the Royal Meteorological Society*, **83 (355)**, 21–29, doi:10.1002/qj.49708335503, URL https://rmets.onlinelibrary.wiley.com/doi/abs/10.1002/qj.49708335503, https://rmets.onlinelibrary.wiley.com/doi/pdf/10.1002/qj.49708335503.

Riley, E. M., B. E. Mapes, and S. N. Tulich, 2011: Clouds associated with the Madden–Julian oscillation: A new perspective from CloudSat. *Journal of the Atmospheric Sciences*, **68 (12)**, 3032–3051, doi:10.1175/JAS-D-11-030.1.

Riley Dellaripa, E. M., E. Maloney, and S. C. van den Heever, 2018: Wind–flux feedbacks and convective organization during the November 2011 MJO event in a high-resolution model. *Journal of the Atmospheric Sciences*, **75 (1)**, 57–84.

Ritchie, E. A., and G. J. Holland, 1999: Large-scale patterns associated with tropical cyclogenesis in the western Pacific. *Monthly Weather Review*, **127 (9)**, 2027–2043.

Roundy, P. E., 2008: Analysis of convectively coupled Kelvin waves in the Indian Ocean MJO. *Journal of the Atmospheric Sciences*, **65 (4)**, 1342–1359.

Roundy, P. E., C. J. Schreck III, and M. A. Janiga, 2009: Contributions of convectively coupled equatorial Rossby waves and Kelvin waves to the real-time multivariate MJO indices. *Monthly Weather Review*, **137 (1)**, 469–478.

Saleeby, S. M., and W. R. Cotton, 2004: A large-droplet mode and prognostic number concentration of cloud droplets in the Colorado State University Regional Atmospheric Modeling System (RAMS). Part I: Module descriptions and supercell test simulations. *Journal of Applied Meteorology*, **43 (1)**, 182–195.

Saleeby, S. M., and S. C. van den Heever, 2013a: Developments in the CSU-RAMS aerosol model: Emissions, nucleation, regeneration, deposition, and radiation. *Journal of Applied Meteorology and Climatology*, **52 (12)**, 2601–2622, doi:10.1175/JAMC-D-12-0312.1.

Saleeby, S. M., and S. C. van den Heever, 2013b: Developments in the CSU-RAMS aerosol model: Emissions, nucleation, regeneration, deposition, and radiation. *Journal of Applied Meteorology and Climatology*, **52 (12)**, 2601–2622.

Seo, K.-H., and H.-J. Lee, 2017: Mechanisms for a PNA-like teleconnection pattern in response to the MJO. *Journal of the Atmospheric Sciences*, **74 (6)**, 1767–1781, doi:10.1175/JAS-D-16-0343.1.

Slingo, J., D. Rowell, K. Sperber, and F. Nortley, 1999a: On the predictability of the interannual behaviour of the Madden–Julian Oscillation and its relationship with El Niño. *Quarterly Journal of the Royal Meteorological Society*, **125 (554)**, 583–609.

Slingo, J., D. Rowell, K. Sperber, and F. Nortley, 1999b: On the predictability of the interannual behaviour of the Madden–Julian Oscillation and its relationship with El Niño. *Quarterly Journal of the Royal Meteorological Society*, **125 (554)**, 583–609.

Smagorinsky, J., 1963: General circulation experiments with the primitive equations: I. The basic experiment. *Monthly weather review*, **91 (3)**, 99–164.

Son, S.-W., Y. Lim, C. Yoo, H. H. Hendon, and J. Kim, 2017: Stratospheric control of the Madden-Julian Oscillation. *Journal of Climate*, **30 (6)**, 1909–1922, doi:10.1175/JCLI-D-16-0620.1.

Stan, C., D. M. Straus, J. S. Frederiksen, H. Lin, E. D. Maloney, and C. Schumacher, 2017: Review of tropical-extratropical teleconnections on intraseasonal time scales. *Reviews of Geophysics*, **55 (4)**, 902–937.

Straub, K. H., and G. N. Kiladis, 2002: Observations of a convectively coupled Kelvin wave in the eastern Pacific ITCZ. *Journal of the Atmospheric Sciences*, **59 (1)**, 30–53.

Straub, K. H., and G. N. Kiladis, 2003: The observed structure of convectively coupled Kelvin waves: Comparison with simple models of coupled wave instability. *Journal of the atmospheric sciences*, **60 (14)**, 1655–1668.

Thayer-Calder, K., and D. A. Randall, 2009: The role of convective moistening in the Madden–Julian oscillation. *Journal of the Atmospheric Sciences*, **66 (11)**, 3297–3312.

Thompson, D. W. J., M. P. Baldwin, and J. M. Wallace, 2002: Stratospheric connection to Northern Hemisphere wintertime weather: Implications for prediction. *Journal of Climate*, **15 (12)**, 1421–1428, doi:10.1175/1520-0442(2002)015<1421:SCTNHW>2.0.CO;2.

Ventrice, M. J., M. C. Wheeler, H. H. Hendon, C. J. Schreck, C. D. Thorncroft, and G. N. Kiladis, 2013: A modified multivariate Madden-Julian Oscillation index using velocity potential. *Monthly Weather Review*, **141 (12)**, 4197–4210, doi:10.1175/MWR-D-12-00327.1.

Vincent, C. L., and T. P. Lane, 2018: Mesoscale variation in diabatic heating around sumatra, and its modulation with the Madden–Julian Oscillation. *Monthly Weather Review*, **146 (8)**, 2599–2614, doi:10.1175/MWR-D-17-0392.1.

Waliser, D. E., R. Murtugudde, and L. E. Lucas, 2004: Indo-Pacific Ocean response to atmospheric intraseasonal variability: 2. Boreal summer and the Intraseasonal Oscillation. *Journal of Geophysical Research: Oceans*, **109 (C3)**.

Wallace, J., 1971: Spectral studies of tropospheric wave disturbances in the tropical western Pacific. *Reviews of Geophysics*, **9 (3)**, 557–612.

Wand, J., H.-M. Kim, E. K. M. Chang, and S.-W. Son, 2018: Modulation of the MJO and North Pacific storm track relationship by the QBO. *Journal of Geophysical Research: Atmospheres*, **123 (8)**, 3976–3992, doi:10.1029/2017JD027977.

Wang, B., 2002: Rainy season of the Asian–Pacific summer monsoon. *Journal of Climate*, **15 (4)**, 386–398.

Wang, B., and X. Xie, 1997: A model for the boreal summer intraseasonal oscillation. *Journal of the Atmospheric Sciences*, **54 (1)**, 72–86.

Webster, P. J., and J. R. Holton, 1982: Cross-equatorial response to middle-latitude forcing in a zonally varying basic state. *Journal of the Atmospheric Sciences*, **39 (4)**, 722–733, doi:10.1175/1520-0469(1982)039<0722:CERTML>2.0.CO;2.

Wheeler, M., and G. N. Kiladis, 1999: Convectively coupled equatorial waves: Analysis of clouds and temperature in the wavenumber–frequency domain. *Journal of the Atmospheric Sciences*, **56 (3)**, 374–399.

Wheeler, M., G. N. Kiladis, and P. J. Webster, 2000: Large-scale dynamical fields associated with convectively coupled equatorial waves. *Journal of the Atmospheric Sciences*, **57 (5)**, 613–640.

Wheeler, M. C., and H. H. Hendon, 2004: An all-season real-time multivariate MJO index: Development of an index for monitoring and prediction. *Monthly Weather Review*, **132 (8)**, 1917–1932.

Wheeler, M. C., H. H. Hendon, S. Cleland, H. Meinke, and A. Donald, 2009: Impacts of the Madden-Julian oscillation on Australian rainfall and circulation. *Journal of Climate*, **22 (6)**, 1482–1498, doi:10.1175/2008JCLI2595.1.

Wu, M.-L. C., S. D. Schubert, M. J. Suarez, P. J. Pegion, and D. E. Waliser, 2006: Seasonality and meridional propagation of the MJO. *Journal of climate*, **19 (10)**, 1901–1921.

Xu, H., S.-P. Xie, Y. Wang, W. Zhuang, and D. Wang, 2008: Orographic effects on South China Sea summer climate. *Meteorology and Atmospheric Physics*, **100 (1-4)**, 275–289.

Xu, W., and S. A. Rutledge, 2014: Convective characteristics of the Madden–Julian oscillation over the central Indian Ocean observed by shipborne radar during DYNAMO. *Journal of the Atmospheric Sciences*, **71 (8)**, 2859–2877.

Yanai, M., T. Maruyama, T. Nitta, and Y. Hayashi, 1968: Power spectra of large-scale disturbances over the tropical Pacific. *Journal of the Meteorological Society of Japan. Ser. II*, **46 (4)**, 308–323.

Yang, D., and A. P. Ingersoll, 2011: Testing the hypothesis that the MJO is a mixed Rossby–gravity wave packet. *Journal of the Atmospheric Sciences*, **68 (2)**, 226–239.

Yang, G.-Y., B. Hoskins, and L. Gray, 2012: The influence of the QBO on the propagation of equatorial waves into the stratosphere. *Journal of the Atmospheric Sciences*, **69 (10)**, 2959–2982, doi:10.1175/JAS-D-11-0342.1.

Yang, G.-Y., and J. Slingo, 2001: The diurnal cycle in the tropics. *Monthly Weather Review*, **129 (4)**, 784–801.

Yu, J.-Y., and S. T. Kim, 2013: Identifying the types of major el niño events since 1870. *International journal of climatology*, **33 (8)**, 2105–2112.

Yuan, J., S. B. Feldstein, S. Lee, and B. Tan, 2011: The relationship between the North Atlantic jet and tropical convection over the Indian and western Pacific Oceans. *Journal of Climate*, **24 (23)**, 6100–6113.

Zangvil, A., and M. Yanai, 1980: Upper tropospheric waves in the tropics. Part I: Dynamical analysis in the wavenumber-frequency domain. *Journal of the Atmospheric Sciences*, **37 (2)**, 283–298.

Zangvil, A., and M. Yanai, 1981: Upper tropospheric waves in the tropics. Part II. Association with clouds in the wavenumber-frequency domain. *Journal of the Atmospheric Sciences*, **38 (5)**, 939–953.

Zhang, C., 2005: Madden–Julian oscillation. *Reviews of Geophysics*, **43 (2)**.

Zhang, C., 2013: Madden–Julian oscillation: Bridging weather and climate. *Bulletin of the American Meteorological Society*, **94 (12)**, 1849–1870.

Zhang, C., and M. Dong, 2004: Seasonality in the Madden–Julian oscillation. *Journal of climate*, **17 (16)**, 3169–3180.

Zhang, C., and J. Gottschalck, 2002: SST Anomalies of ENSO and the Madden–Julian Oscillation in the Equatorial Pacific. *Journal of Climate*, **15 (17)**, 2429–2445, doi:10.1175/1520-0442(2002)015<2429:SAOEAT>2.0.CO;2.

Zhang, C., and B. Zhang, 2018: QBO-MJO connection. *Journal of Geophysical Research: Atmospheres*, **123 (6)**, 2957–2967, doi:10.1002/2017JD028171.

Zhang, G. J., and M. Mu, 2005: Simulation of the Madden–Julian oscillation in the NCAR CCM3 using a revised Zhang–McFarlane convection parameterization scheme. *Journal of Climate*, **18 (19)**, 4046–4064.

Zhang, Y., T. Li, B. Wang, and G. Wu, 2002: Onset of the summer monsoon over the Indochina Peninsula: Climatology and interannual variations. *Journal of Climate*, **15 (22)**, 3206–3221.

Zhou, L., R. B. Neale, M. Jochum, and R. Murtugudde, 2012: Improved Madden–Julian oscillations with improved physics: The impact of modified convection parameterizations. *Journal of Climate*, **25 (4)**, 1116–1136.

Zuluaga, M. D., and R. A. Houze Jr, 2013a: Evolution of the population of precipitating convective systems over the equatorial Indian Ocean in active phases of the Madden–Julian oscillation. *Journal of the Atmospheric Sciences*, **70 (9)**, 2713–2725.

Zuluaga, M. D., and R. A. Houze Jr, 2013b: Evolution of the population of precipitating convective systems over the equatorial Indian Ocean in active phases of the Madden–Julian oscillation. *Journal of the Atmospheric Sciences*, **70 (9)**, 2713–2725.